Università Cattolica del Sacro Cuore
Sede di Brescia

Facoltà di Scienze Matematiche, Fisiche e Naturali
Corso di Laurea Magistrale in Fisica

Tesi di Laurea

Cluster analysis techniques for single nano-object time-resolved optical experiments

Relatore:
Prof. Gabriele Ferrini
Correlatore:
Prof. Francesco Banfi

Laureando: **Andrea Ronchi**
mat. **4204632**

Anno Accademico 2014/2015

A mamma, papà e Matteo

Contents

Chapter 1

Introduction

1.1 Overview

In the last few years the interest in the energy transfer at the nanoscale has considerably grown due to the many technological and biomedical possible applications from the photothermal therapies in oncology [1, 2] to in-situ drug delivery [3]. The fundamental idea underlying these applications is selective thermal energy delivery in form of heat transfer from the metal nanoparticle to the environment. Therefore, an understanding of the thermomechanical dynamics is crucial in view of future applications.

Unfortunately, the development of physical models for such systems is not easy due to their complexity in several aspects. First of all, in a nano-object the chemical and physical properties are essentially different from the macroscopic situation [4, 5]. For example, at the nanoscale, heat and mechanical work are intrinsically correlated concepts.
In second instance, the metal nanoparticles used in biomedical and chemical applications are often embedded in a complex chemical environment. Modeling these chemical bonds and their physical responses could be extremely difficult. For this reason, in recent years, new statistical and mathematical tools are been developed to extract useful informations from the experimental data without previous knowledge of the physical mechanisms of the system. These new analysis techniques are generally named *Data Mining* or *Pattern Recognition*, and are applied in many scientific fields, including signals analysis, meteorology, genomics, complex physics simulations,

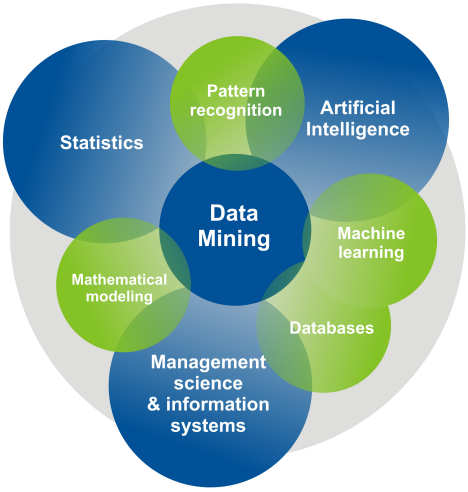

Figure 1.1: What is *Data mining*? Data Mining is a computer based-process for converting large data volumes to information and knowledge by finding patterns within the data using different techniques of visualization, reduction of dimensionality, classification, and construction of models. Data Mining is also an interdisciplinary tool encompassing a blend of statistical, artificial intelligence, and information systems disciplines for pattern recognition, mathematical modeling, and databases activities.

and biological research. In particular, *Data Mining* is a computer based-process for converting large data arrays to information by finding patterns within the data using different techniques of visualization, reduction of dimensionality, classification, and construction of models.

The aim of this thesis work is investigate the thermomechanical dynamics through clustering techniques, starting from single nano-object time-resolved optical measurements. In particular, we are interested in the study of a complex system like gold nanoparticles immobilized on a functionalized surface through the bond between biotin and streptavidin. These results will be compared against a standard analysis based on a sum of exponentially decaying functions and will be shown to provide the best performance.

1.2 Outline

The work is organized as follows. The second chapter explains the basic concepts of time-resolved optical spectroscopy, with particular attention to the pump-probe technique, and the working principle of ASynchronous Optical Sampling (ASOPS)[7, 8]. After that, the experimental setup,

the Nanoscope and the sample's characteristics will be described. The first samples are gold/titanium nanodisks made by electronic beam lithography. The second ones are gold nanoparticles immobilized on a functionalized substrate through the bond between biotin and streptavidin.

The third chapter describes some common clustering and pattern recognition techniques, aim of this thesis work. In particular, the time-resolved spectra will be analyzed using two approaches: a Singular Value Decomposition (SVD) analysis and a hierarchical binary cluster tree dendrogram built using an Euclidean distance (Ward's method). The SVD has many useful applications in signal processing and statistics. The hierarchical cluster analysis is usually used to find relationship in data. Furthermore, these approaches will be compared with a standard data analysis. Appendices were added in order to collect information and annotations.

Chapter 2

Time-resolved spectroscopy

2.1 Optical pump-probe technique with ASOPS

Time-resolved spectroscopy is used to study the thermomechanical dynamics of single nano-objects (in our case, gold nanodisks and gold nanospheres). The thermomechanical relaxation dynamic of these systems spans time scales ranging from 100 ps to 10 ns.

The standard technique that is used to investigate these time scales is the pump-probe based on a mechanical delay line. In this method, a laser is splitted into two beams through a beam splitter. Between the two beams, the one with greater intensity (pump) is used to excite the sample. The second one with lower intensity (probe) is used instead to "photograph" the dynamics of the sample. Since the probe laser beam is much less intense than the pump's one does not substantially excite the sample (Fig. 2.1).

What it is measured directly with this technique is the difference of relative transmission (or relative reflectivity) of a certain material. The optical properties of the material are changed by a perturbation in the electronic structure. This perturbation is given by the pump pulse, the variation in reflectivity is investigated through probe pulses.
If we are able to ensure that the probe pulses arrives on the sample with increasing delays time with respect to pump pulses, we are also able to follow the relaxation dynamic of the sample from the excited state to the unperturbed. To introduce the delay between the pulses, the most used method is a mechanical delay line. This line allows the pump pulse to follow a different

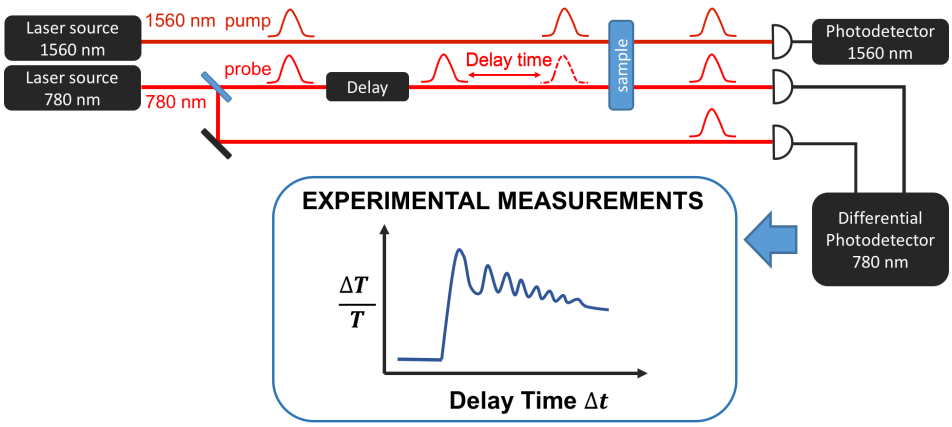

Figure 2.1: Typical pump-probe optical experiment performed on a nano-object. The signal from the probe pulses is detected as the mechanical delay line is being scanned. By the relation $\Delta t = 2\Delta r/c$, c being the speed of light, the position change Δr of the mechanical delay line is translated into a change of the time delay between pump and probe pulse.

optical path so that the two beams arrive on the sample with a relative delay. By controlling the difference in the optical path of the probe beam with respect to the pump beam, the time delay between the two pulses can be tuned. Varying this delay one can access to the relaxation dynamics of the sample.

This technique allows us to perform time-resolved measurements with excellent temporal resolution, however presents different problems when the nano-object's thermomechanical dynamic exceeds the hundreds of *ps*. These are the typical problems [9]:

- A long delay line makes it difficult to maintain the spatial coincidence between the pump beam and the probe.
- The data acquisition is very slow because each time we have to move the slide to change the optical path. Slow acquisition causes problems in terms of stability of the experimental line (thermal fluctuations in the laser, in the optical elements, in temperature in the case of cryogenic measurements, and so on...)
- The problems listed above are intensified if the technique is applied in microscopy. In such case the acceptance on spatial alignment is more stringent.

The above problems can be solved using a pump-probe technique based on ASynchronous

Figure 2.2: Laser source and ASOPS system.

Optical Sampling (ASOPS), that doesn't involve movement of mechanical parts.

2.2 ASOPS working principle

The ASOPS used in this work is composed of two lasers with wavelengths of 780 nm and 1560 nm. The lasers are pulsed with a pulse length of about 150 fs (Fig. 2.2). The repetition rate of the pump laser is 100 MHz. In the probe laser the repetition rate is sligthy detuned with respect to pump one's.

Defining as ν_{pump} and ν_{probe} the frequencies of repetition rate of the two lasers we can determine the delay time between the two:

$$\Delta t = \left| \frac{1}{\nu_{pump}} - \frac{1}{\nu_{probe}} \right| = \frac{\Delta\nu}{\nu_{pump} \cdot \nu_{probe}} \tag{2.1}$$

where $\delta\nu$ is the frequency difference between the two lasers. Supposing that the frequency difference in small and expanding the last equation ($\nu_{probe} = \nu_{pump} + \Delta\nu$) we obtain:

$$\Delta t \approx \frac{\Delta\nu}{\nu_{pump}^2} \tag{2.2}$$

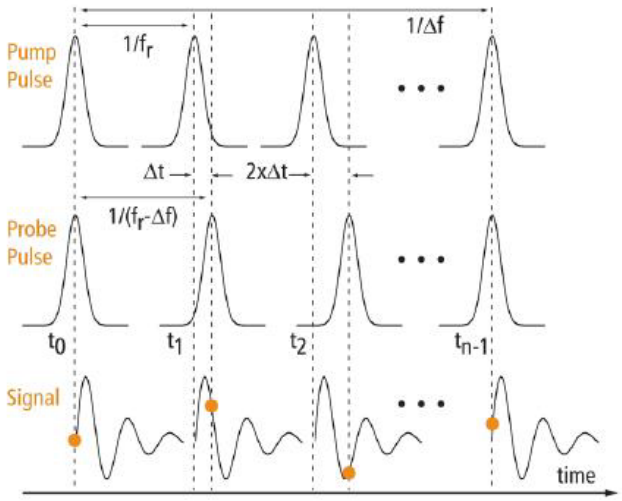

Figure 2.3: Operating principle of the ASOPS technique. In figure is shown the mutual temporal delay between the pump and the probe pulse, defying f_r and $f_r - \Delta f$ respectively. Because of the detuning Δf between the pulses of the two lasers, a progressive temporal delay between them is accumulated which allows to measure the entire relaxing dynamics of the sample.

Eq. 2.2 defines the temporal step of a pump-probe measurement. Considering a typical frequency detuning of 10 KHz, we get a resolution of 10^{-12} s . The temporal window sampled is obtained by the following formula:

$$t_{window} = \frac{1}{\nu_{pump}} = \frac{1}{100\ MHz} = 10\ ns \tag{2.3}$$

Now we want evaluate the time it takes to perform a pump-probe measurement. The probe pulse accumulates a delay Δt for each pump pulse, until they meet again after a fixed time interval t_0.

The operating principle of the ASOPS frequency detuning is represented schematically in Fig. 2.3. We estimate t_0. How many pulses of probes are needed to cover the interval between two successive pump pulses? Defining m as the number of pulses that we are looking for:

$$m\Delta t = \frac{1}{\nu_{pump}} \tag{2.4}$$

where in the right-hand side there is the distance in time between two successive pump pulses.

Recalling the equation 2.2:

$$\frac{m\Delta\nu}{(\nu_{pump})^2} = \frac{1}{\nu_{pump}} \tag{2.5}$$

so

$$m = \frac{\nu_{pump}}{\Delta\nu} \tag{2.6}$$

The value of t_0 is related to m as follows:

$$t_0 = m\left(\frac{1}{\nu - \Delta\nu}\right) \tag{2.7}$$

Substituting m from equation 2.5 in 2.7 we get:

$$t_0 = \left(\frac{\nu_{pump}}{\Delta\nu}\right)\frac{1}{\nu_{pump}}$$

$$t_0 \simeq \frac{1}{\Delta\nu} \tag{2.8}$$

The management of the temporal delay between the two lasers pulses eliminates the problems that characterize the traditional pump-probe method. In fact, if we don't need to give a mechanical delay, we have no trouble keeping spatially coincident the two lasers beams. With conventional techniques, the time needed to investigate a single time window of 10 ns with a temporal resolution of 150 fs involves an acquisition time of the order of an hour, with ASOPS the same measurement is made in 1 ms.

As regards the temporal window, with the traditional technique you typically have a dynamic range of the order of ns or less, using the ASOPS the temporal window is increased by one order of magnitude, or 10 ns.

2.3 Experimental setup

2.3.1 Optical lines

The experimental setup shown in Fig. 2.4 has been studied for time-resolved optical microscopy measurements on nanostructured samples. Laser sources, Nanoscope and detectors are rapp-

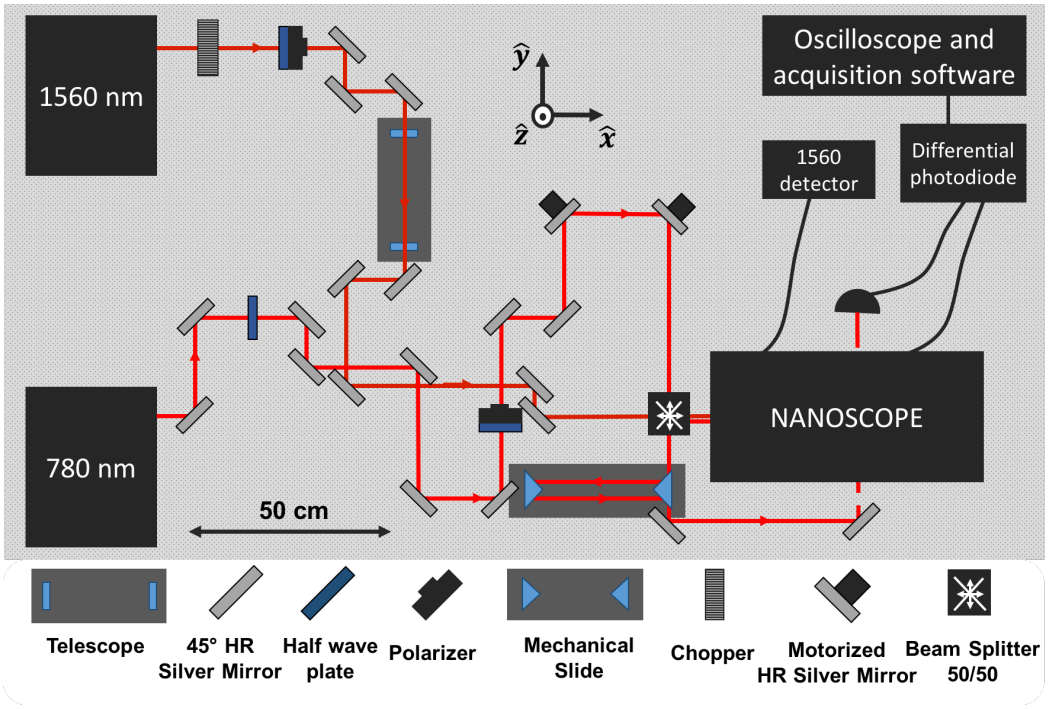

Figure 2.4: Scheme of the experimental setup. Under: the optical lines's legend.

resented as black boxes with an input and an output. Mirrors and lens have a characteristic representation and the complete legend is reported below figure.

To generate the pulses at 1560 nm for our experiments we used a erbium doped fibre laser, guided in the nanoscope through a system of optical elements. An half-wave plate coupled with a polarizer allows to settle the intensity of the beam, while the passage through two convex lenses of focal lenght 40 cm and 20 cm, f_1 and f_2 respectively, forming an expanding telescope, expands the diameter of beam. Before the pump beam enters the nanoscope, it passes through a pinhole of variable radius. The beam is detected by a photodetector (in Fig. 2.4, labelled as "1560"). The probe beam, at 780 nm, is splitted by a 50/50 beam splitter. It produces two beams at 780 nm: a probe beam, that enters in the nanoscope, and the reference one, driven to the differential photodetector [1].

A mechanical slide supporting two mirrors, allow us to vary this line, so that we can set the temporal overlapping of the probe beam trasmitted through the sample and the unperturbed one, before entering the photodetector, which is fundamental in order to acquire the difference

[1] see appendix for more information.

between these signals.

Both pump and probe laser beams outgoing from the nanoscope are collected by parabolic mirrors and transported to the photodetector by an optical fiber.

2.3.2 Nanoscope

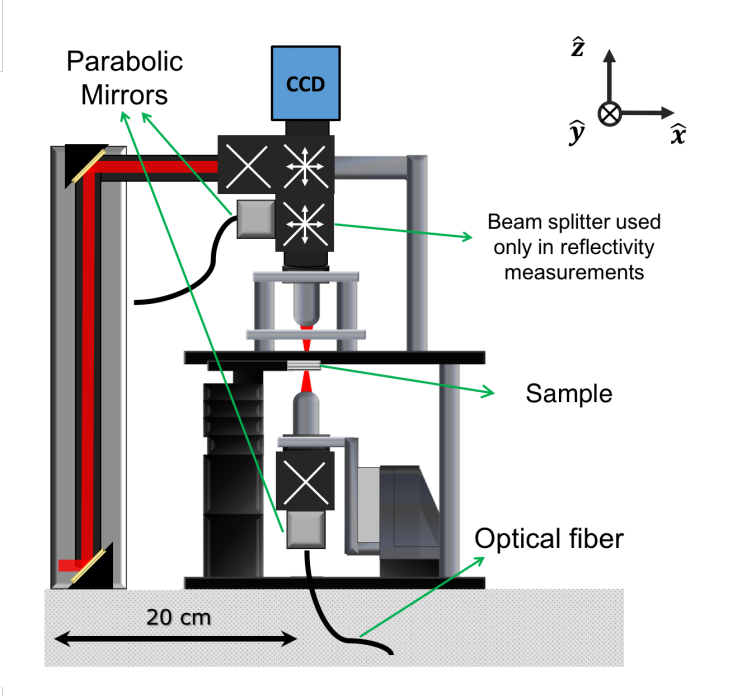

Figure 2.5: Nanoscope's structure and beams' path

In this subsection it is explained the structure of the nanoscope, together with the common path of pump and probe beams. (Fig. 2.5). This tool is composed by two mirrors, a 50/50 beam splitter, two objectives and a CCD camera.

After the beam enters in the nanoscope, the two gold mirror reflect the beams on the 50/50 beam splitter. This serves to direct the beam into a 50x Nikon objective. The divergent beam, transmitted through the sample, is collected by an identical objective. After that, the outgoing beams are collected by parabolic mirrors and they are guided to the photodiodes by means of optical fibers. In the case of reflectivity measures, a supplementary 50/50 beam splitter allows to split the reflected probe toward a fiber linked with the differential photodiode[2].

[2]For more details on differential photodetector, see Appendix A.1.1.

The advantages of using the nanoscope:

- The size of probe beam's spot (1 μm) facilitates the detection of objects characterized by dimensions much lower than wavelenght of laser beam. If the distance between two nanoparticles on the sample is similar to the size of laser's spot, it could be easier to identify the single particle focusing the probe beam to the diffraction limit. To do this, we have to apply some optical techniques as the *raster-scan*, described (qui sotto).

- Characterization and spatial control of the position of laser beams. By means of the nanoscope, it is possible to retrace the spatial distribution of beams, focus the beam on the xy plane in which the sample lies, and also evaluate the angle of beam with respect to z axis.

- Optimization of beams to perform pump-probe measurements. Since that the profiles of the laser beams are gaussian, it is easy to calculate the energy density at different z planes for each of the two beams. It is also possible to locate the mutual position of beams in order to make them collinear, incident on the sample and directed along the z axis. Due to the chromatic aberration of the first objective, the probe beam is focused higher with respect the pump beam. This represents a great advantage in the current setup. On the sample, the pump spot is larger than the probe spot. This assure that we are probing an uniformly excited area of the sample.

These things are fundamental to allow the correct positioning of beams on the nano-object. The aim of this work is the analysis of the power transmitted through a single or group of nano-objects at the position (x_0, y_0) on a surface, defined as

$$P_t = P_i - \sigma_{ext} \cdot I(x_0, y_0) \tag{2.9}$$

where P_i is the incident power on the sample, σ_{ext} is the effective cross section and $I(x_0, y_0)$ is the intensity spatial profile. The second term on the right-hand side represents a power and takes into account both the energy absorbed and scattered by the sample. The photodetector gives a signal in terms of voltage and to identify the signal coming from the nanoparticles is

necessary to do a sequence of translations, the so-called *raster scan*, that allows to create an image, that represents the beam reconstructed using the nano-object. Indeed, when the probe beam, whose spot is much bigger than the characteristic size of particles, passes on a nano-object, the system records a variation of transmitted power given by the convolution of the Gaussian function, corresponding to the beam, and a Dirac delta function, associated to the particle.

2.4 Samples

In this section, we want to describe the structure of our samples. Their position in the nanoscope has been indicated in Fig. 2.5.

2.4.1 Gold/titanium nanodisks

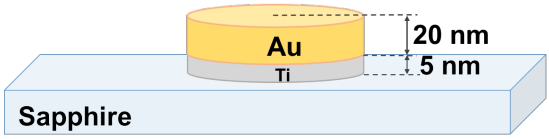

Figure 2.6: Single gold/titanium nanodisk geometry.

The sample was made using the electronic lithography at the *Lasim*[3] and consists of a monocrystalline sapphire substrate (Al_2O_3) (R-plane cut, size 10 mm x 10 mm and thickness of 127 μm) on which are deposited aluminium structures (Al) (Fig. 2.7). This makes it possible to identify the correct position of the nanodisks on the sample through the optical technique already mentioned in the previous section (*raster scan*). The sapphire plate has the merit to be a transparent dielectric (refractive index $n_z = 1.77$ @ 780 nm e $n_z = 1.74$ @ 1560 nm [10]) with thermal conductivity $k = 20\ \frac{W}{m \cdot K}$ @ $300K$. The choice of a transparent medium with a low k facilitates physical interpretation because it allows to consider the sapphire " almost" isothermal during the heat exchange process between nanodisk and substrate.

Gold nanodisks are evaporated on this sapphire plate. Between the nanodisk and the substrate, it is interposed an adhesive layer of titanium. The Fig. 2.6 shows the thickness and the

[3]Laboratoire de Spectrometrie Ionique et Moleculaire, Lyon, France

geometry of the single disk. We have five different diameter sizes: 60, 70, 80, 90, and 100 *nm*. (Fig. 2.7)

The disks of each measure are placed in different sectors according with the dosage of the electron beam[4]. The Fig. 2.8 shows a schematic illustration of a typical sub-area characterized by disks of a given diameter and dosage, and it consists of 16 disks surrounded by rectangular markers.

In this work we performed different measurements on single nanodisks of 90 and 100 *nm* diameters.

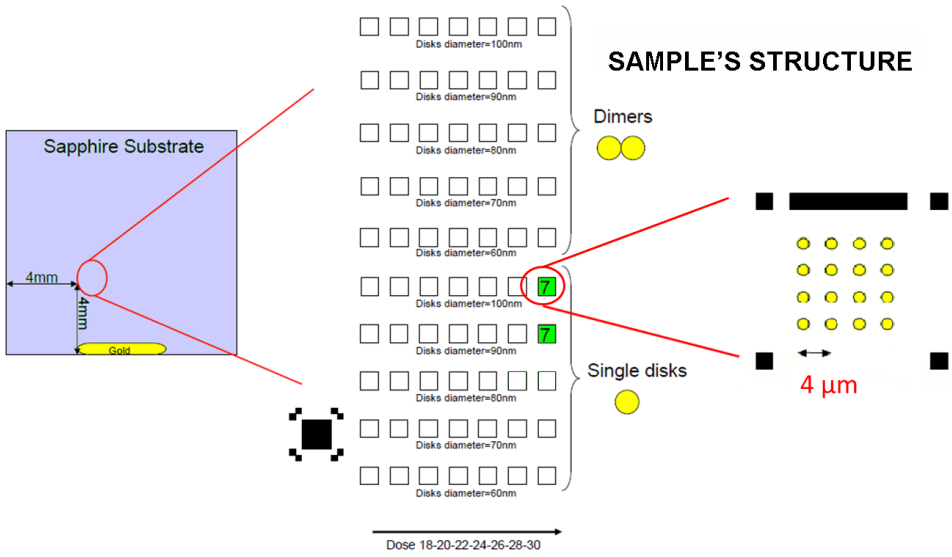

Figure 2.7: The template of the nanodisks' sample. The nanodisks are organized for dimension and electronic dose.

[4]for more information about the definition of dose in EBL, see: *http://en.wikipedia.org/wiki/Electron_beam_lithography*. The above mentioned values are normalized to a reference dose and are therefore dimensionless.

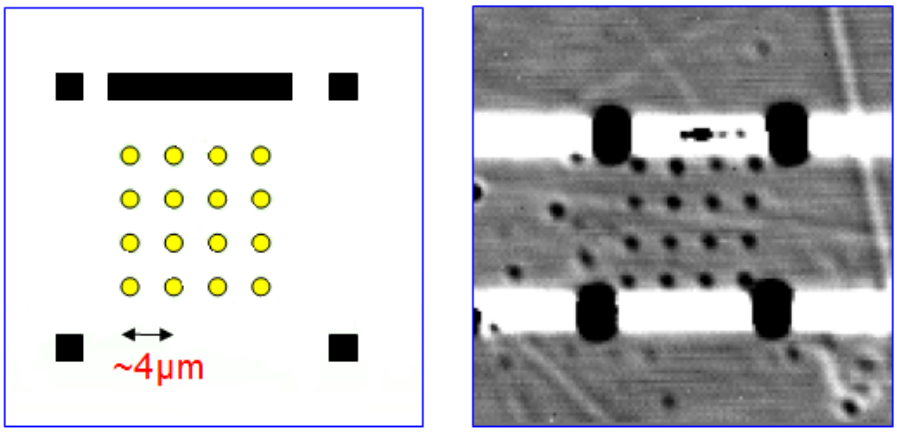

Figure 2.8: Left: Schematic representation of a single zone. Right: An optical scanning image of dimensions 30 $\times$ 30 μm, disk's diameter = 100nm and maximum dose.

2.4.2 Gold nanospheres

The substrate has been realized at *NEST Laboratory*[5] and consists of a sapphire (Al_2O_3) plate (diameter 12 mm, thickness 180 μm), on which are nanolitographed Cr/Au 10 nm/100 nm markers, required to localize nanoparticles on the sample. In Figg. 2.9 - 2.10, markers's templates are sketched. On this substrate, after its functionalization, gold nanospheres have been immobilized.

The functionalization of our samples has been realized at *ICRM-CNR*[6], by deposition of streptavidin conjugated gold nanoparticles[7] on the substrate. The average diameter of these nanospheres is 40 nm. We are now going to explain the procedure followed to coat the slides.
After 15 minutes of oxygen plasma treatment, sapphire substratum were immersed for 30 minutes in a 0.9 M ammonium sulfate solution (half volume of H_2O, half volume of NH_4SO_4) containing poly (DMA-co-NAS-co-MAPS)[8]at 1% w/v concentration.[9]
The covered substrates were left for 20 minutes immersed in the polymer solution and then rinsed with water, dried with nitrogen and finally cured under vacuum at 80° for 15 minutes. The last

[5]National Enterprise for nanoScience and nanoTechnology, Pisa, Italy
[6]Istituto di Chimica del Riconoscimento Molecolare-Consiglio Nazionale delle Ricerche, Milan, Italy
[7]Made by Cytodiagnostics, Burlington, Ontario, Canada
[8]For the synthesis of copoly refer to [11]
[9]The 1% concentration, expressed through the ratio weight/volume, means that there is 1 g of solute for 100 ml of solution

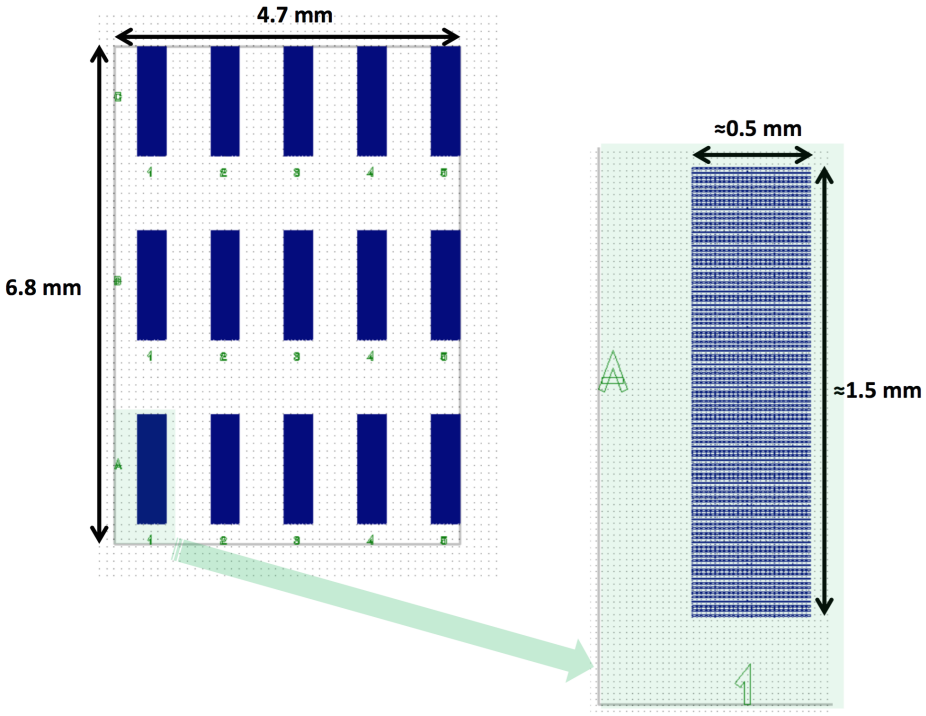

Figure 2.9: Scheme of a template (4.7 mm × 6.8 mm), characterized by macro-areas or clusters (0.5 mm × 1.5 mm). This particular construction allows to spot different antibody concentration on each clusters.

passage, named *curing*, in addition to dry the sample, facilitates the creation of a strong bond between the polymer and the surface.

When the sample has been dried, biotinylated antibody was patterned on sapphire substrates[10] coated with polymer. The antibody was diluited in PBS[11] with four different concentrations and the solution was spotted on the sample. The slides were placed in a humid chamber immediately after the spotting and stored overnight at room temperature. After immobilization, the residual active esters on the slides were blocked with a blocking solution (ethanolamine) for 1 hour, washed with water and dried by a stream of nitrogen. After that, the spotted substrates were then incubated with a solution of gold nanospheres conjugated with streptavidin at different concentrations for 1 hour, washed with the Washing Buffer for 10 minutes under stirring and

[10]Made by means of SciFlexArrayer S5 spotter from Scienion (Berlin, Germany). The diameter of the spot is about 150 μm

[11]Phosphate Buffered Saline

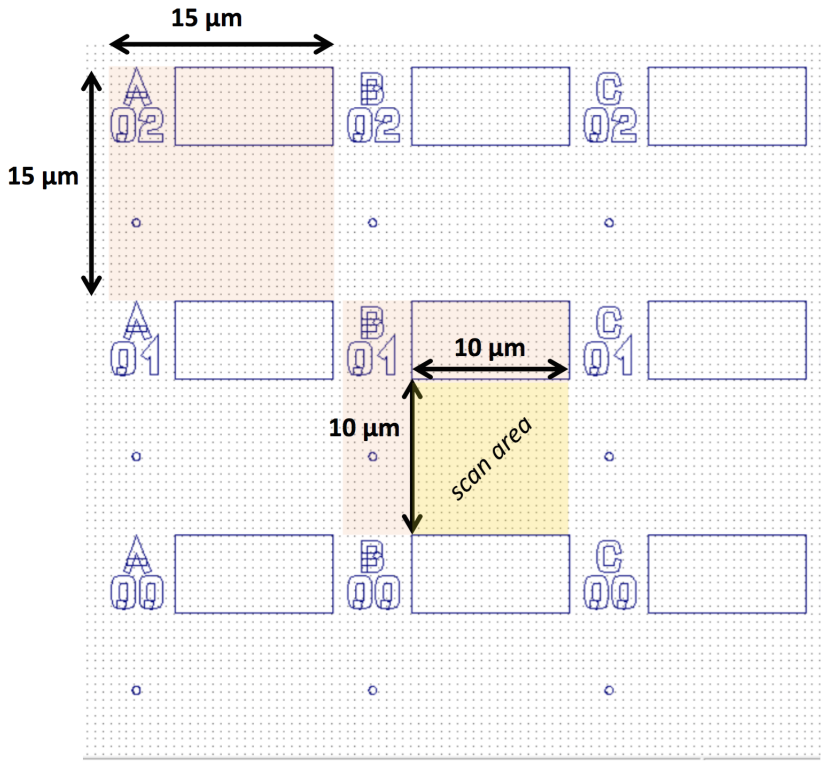

Figure 2.10: Each marker that identifies a macro-area is divided in cells (15 μm $\times$ 15 μm), named with a letter and a number and characterized by a scan area of 10 μm $\times$ 10 μm, a gold edge and a dot (diameter 500 nm). This makes it possible to identify the correct position of the particles on the sample through the optical technique already mentioned in the previous section (*raster scan*)

finally rinsed with water and dried with nitrogen. (see Fig. 2.11)

In this work we measured and analyzed two sample's areas with different concentrations of nanoparticles and antibody: (1) sample A - cluster 4 with nanoparticles diluted 1:10 with respect to the manufacture's dilution and 0.1 mg/ml antibody, (2) sample E - cluster C3 with nanoparticles undiluted with respect to the manufacture's dilution and 1 mg/ml antibody.

It is important to highlight that the gold nanospheres are a much more complex system to study. Their modeling through simple analytical models is almost impossible, because the microscopic arrangement and physical response of streptavidin-biotin bonding is unknown. In fact, depending on the different dilutions of antibody and nanoparticles, these could clustering into groups or the chemical enviroment could be different.

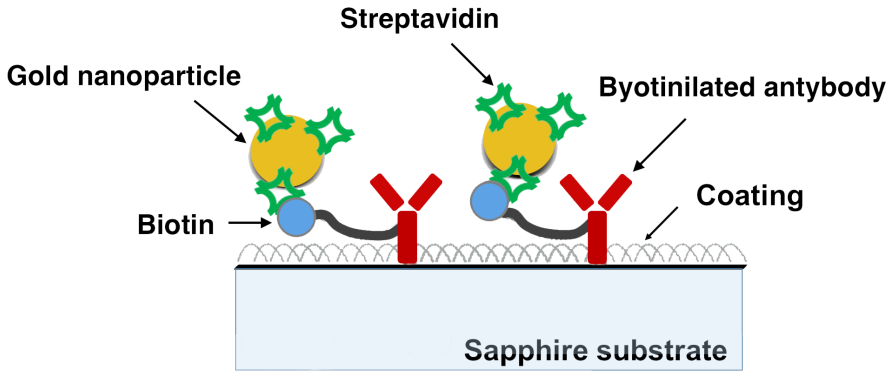

Figure 2.11: Schematic rappresentation of the streptavidin-biotin bonding that has been used to immobilize the nanoparticles on the sapphire substrate.

2.5 Operating procedures

This section presents the procedures that are required to perform time-resolved pump-probe measurements by means of the Nanoscope.

To obtain the best measurement, it is fundamental that both pump and probe beams are parallel and coaxial on the nano-object. Below we summarize the main steps that are required:

- **Alignment of laser beams**

  Pump and probe beams are collimated and spatially overlapped before entering in the Nanoscope. In fact, the spatial coincidence of the beams' pulses is required.

- **Nanoscope's optimization**

  Our goals is to drive pump and probe beams through the two 50X Nikon's lenses. It is important that the distance between the two optics and the sample is the same.

- **Research of the minimum waist**

  We want to determinate the minimum waist w_0 of the probe beam using knife-edge technique[12]. Along z axis, the sample will be placed in w_0 (see Fig. 2.5)

- **Positioning on the single nano-object**

  By means of the program "SPM Control", it has been possible to achieve a so-called *raster*

[12]For more informations on knife-edge technique, see Medeghini and Sterzi's thesis[7, 8]

scan of the sample. This process allow us to obtain a square "map" of the sample. This image is defined as the imaging of the beam. Through this imaging it has been possible to align the laser beams on a single nano-object[13].

All these steps are the same both in the case of nanodisks that in that the nanospheres.

[13]For more informations on positioning techniques, see Medeghini and Sterzi's thesis[7, 8]

2.6 Time-resolved pump-probe measurements

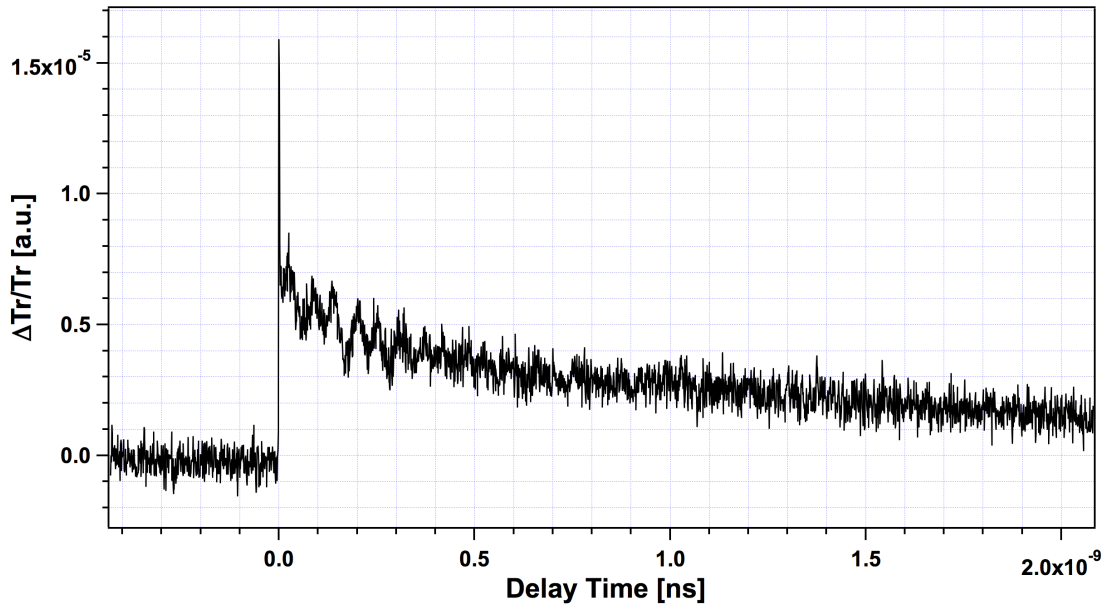

Figure 2.12: Relative variation of transmission versus time delay measured on a single nanodisk of 100 nm diameter. Pump's power is 61 mW, probe's one is 470 μW. The probe's FWHM is 1.05 μm. The detuning is set to $\Delta\nu = 10\ KHz$ with a temporal resolution of 1 ps.

Once the beams are correctly positioned on the nano-object, we begin to measure with the Asops system. The pump's pulse excites the nano-object (in our case, a nanodisk or a nanosphere), delivering the energy density dU. We can identify three different temporal dynamics, corresponding at three different time scales.

In a first step, the absorbed energy produces the heating of electron gas of the metallic nanostructure (subpicosecond time scale). In fact, the electromagnetic energy is absorbed by the electrons, as in the Drude model.

After that, the electrons thermalize with the lattice's phonons by means of scattering processes (picosecond time scale). The effect is an increase of lattice's temperature from T to $T + \Delta T$, that causes a thermal expansion of the nanostructure itself. As a result of electron's heating, there is a change in the dielectric constant and a variation of nano-object's size, leading to an increase of the extinction cross section of the object exposed to the probe beam. Therefore, we measure a decrease of beam's transmitted power, according to Eq. 2.9.

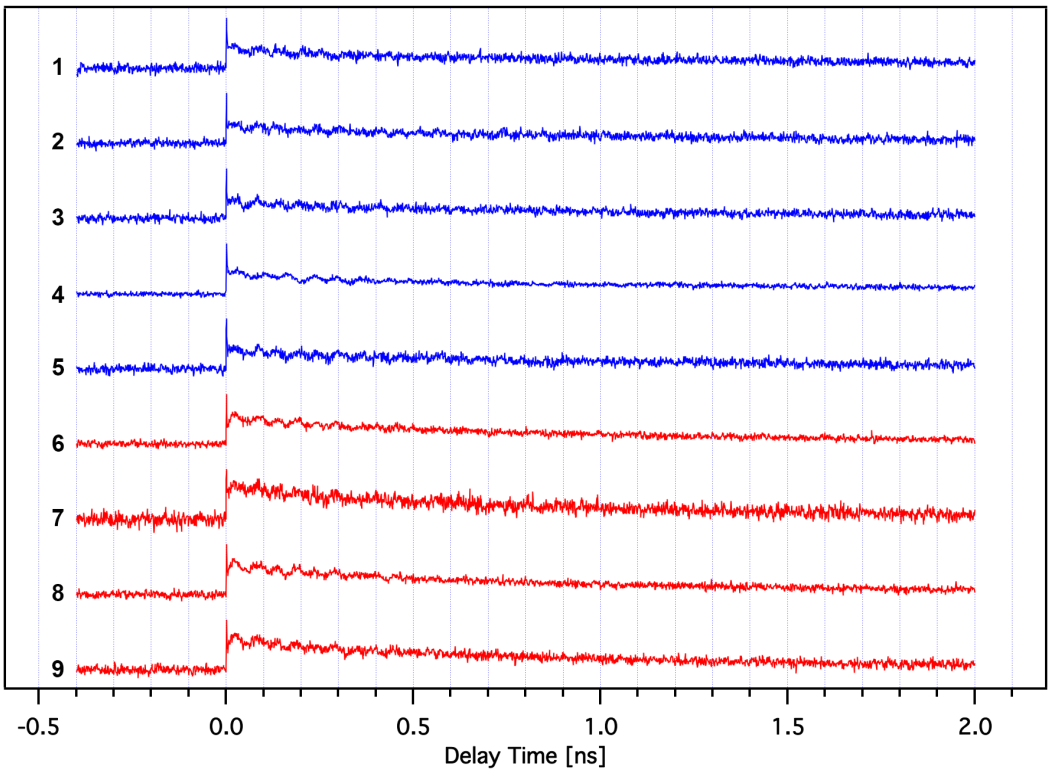

Figure 2.13: Blue spectra: Relative variation of transmission versus time delay measured on a 100 nm single-nanodisk. Red spectra: Relative variation of transmission versus time delay measured on a 90 nm single-nanodisk. Pump's power is 61 mW, probe's one is 470 μW. The probe's FWHM is 1.05 μm. The detuning is set to $\Delta\nu$=10 KHz with a temporal resolution of 1 ps. The curves have been normalized with respect to the maximum value and they have been restricted to a temporal range up to 2 ns.

At the end, there is the energy's relaxation of the nano-object with the substrate (nanosecond time scale). In this step the energy density dU absorbed by the nano-object is transferred to the substrate by mechanical and thermal dissipation channels.

As the dissipating processes take place and the extinction cross section reaches the unperturbed value, the nanostructure slowly returns to its thermomechanical equilibrium. This leads to a decrease of relative transmittance ΔTr/Tr, that amounts to zero when the particle is completely thermalized with the substratum at temperature T. Together with the typical exponential decay will be observed even an oscillation in the relative transmittance ΔTr/Tr due to the launching of an acoustic mode in the nanostructure. (see Fig. 2.12)

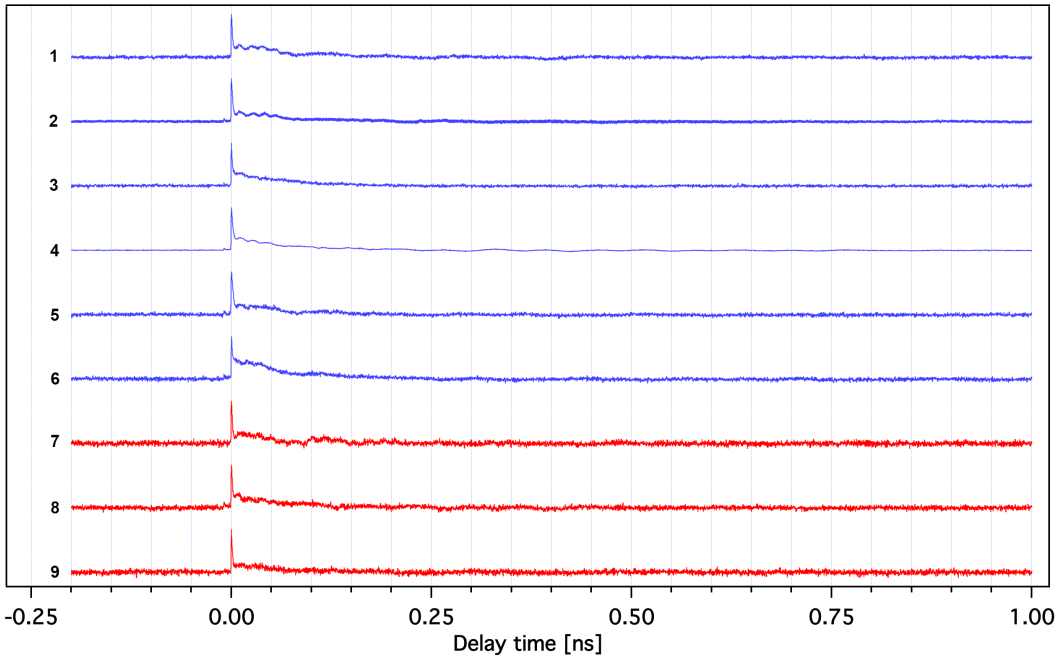

Figure 2.14: Blue spectra: Relative variation of transmission versus time delay measured on a single-nanosphere (sample E). Red spectra: Relative variation of transmission versus time delay measured on on a single-nanosphere (sample A). Pump's power is 3 mW, probe's one is 200 μW. The probe's FWHM $\sim$ 1 μm. The detuning is set to $\Delta\nu$=1 KHz with a temporal resolution of 100 fs. The curves have been normalized with respect to the maximum value and they have been restricted to a temporal range up to 1 ns.

The variation of transmitted power, ΔTr, is proportional to the voltage provided by the "RF-OUTPUT" channel of the differential photodetector, while the value of absolute transmitted power, Tr, is proportional to the one measured by the "MONITOR+" channel. Because of the different conversion of the two channels, there is an intrinsic conversion factor that has to be taken in account. As we are interested in the relaxation time of the sample, the exact value of the ratio is not significant, therefore an error due to this conversion factor can be neglected.
The first step of the measurement consists in measuring ΔTr, averaged on n temporal scans. The value ΔTr provided by the photodetector must be divided by the voltage of probe's beam in absence of pump one, Tr, in order to obtain a relative variation.

In Figg. 2.13 and 2.14 we show all the curves obtained through the measures, and that will be analyzed in the next chapter. The curves are normalized with respect to the maximum value. Note that the numeration used it will be found in the analysis of the next chapter.

Chapter 3

Data mining and clustering techniques

We analyze the thermomechanical properties of gold nanoparticles immobilized on a functionalized surface through the bond between biotin and streptavidin, which is characterized by high affinity and binding energy.

Starting from the pump-probe measurements that have been shown in the previous chapter, we study the thermomechanic of these complex systems without previous knowledge of the physical mechanisms responsible for the detected signal. For this purpose we use mathematical and statistical tools, rather than curve fitting analysis. In fact, in order to apply a curve fitting analysis we need a theoretical model, from which it is possible to obtain a functional trend. In our system the microscopic molecular arrangement and physical response of streptavidin-biotin bonding is unknown. Depending on the different dilutions of antibody and nanoparticles, these cluster into groups and the chemical enviroment could be different.

A typical approach to this kind of biological complex systems is known as data mining or pattern recognition. The overall goal of our data mining process is to extract useful information from experimental data and sort out the differences among different dilution of samples. One possibility is to organize the measures into groups by similarity. These ordered data sets are called clusters.

In this thesis work, the time-resolved spectra are analyzed using two clustering approaches: 1)

a Singular Value Decomposition (SVD) analysis, 2) a hierarchical binary cluster tree dendrogram built using an euclidean distance (Ward method). These approaches are compared against the standard analysis based on the sum of exponentially decaying functions and are shown to provide the best performance.

First of all, we try to apply these techniques to well-known nanostructures like gold nanodisks coupled with an isothermal substrate[1], for which an analytical model for the thermomechanical dynamic is already been developed[12, 19]. Next, we will focus on the gold nanospheres, once it has been demonstrated the effectiveness of the technique for our purposes.

3.1 Gold/titanium nanodisks

3.1.1 Singular Value Decomposition

In this section we describe the use of Singular Value Decomposition (SVD) in analyzing time-resolved optical measurements on single gold nanodisks shown in Fig. 2.13. The dynamics measured on the disks with different dimensions looks very similar, the signature of the specific time-response residing in tiny differences. The total 9 normalized measurements have been organized in a $m \times n$ data matrix[2] X with rank[3] r. The nth column represents a complete experimental trace. The mth row maps a time delay for each trace. It is important noting that the traces are affected by evident fluctuations of the noise superposed on the exponential decay dynamic due to the different experimental conditions (temperature, humidity, laser's fluctuations, ecc).

SVD is a linear transformation of the expression from the m-delays $\times$ n-traces space to reduced $l \times l$ space, where $l = \min\{n,m\}$. In particular, the data matrix is expanded in the form

$$X = USV^T [20]. \tag{3.1}$$

U is a matrix with the same dimensions as X matrix ($m \times n$) whose columns are called *left singular eigenvectors* $\mathbf{u_k}$. Since $\{\mathbf{u_k}\}$ form an orthonormal basis for time-resolved measurements,

$$\mathbf{u_i} \cdot \mathbf{u_j} = \delta_{ij}. \tag{3.2}$$

[1] In the case of sapphire, the thermal conductivity k is 20 $\frac{W}{m \cdot K}$ @ $300K$, and so the substrate can be considered as a transparent medium.

[2] For the nanodisks' measurements, we have a 2000×9 data matrix X.

[3] The *rank* of a matrix is the number of linearly independent rows or columns.

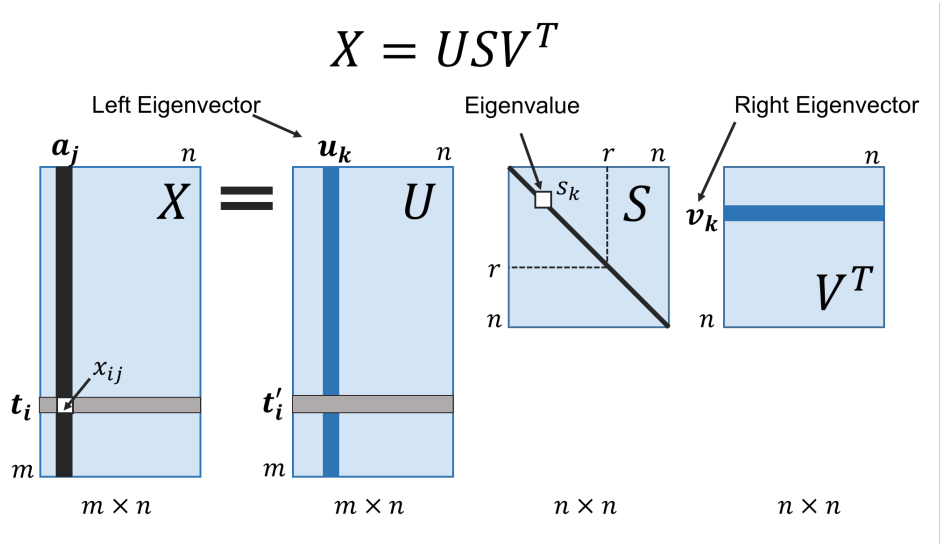

Figure 3.1: Graphical depiction of SVD of a matrix X, annotated with notation adopted in this chapter.

These eigenvectors $\{\mathbf{u_k}\}$ are found by minimizing the variance between the residues of each experimental trace and a direction (eigenvector) in a n-dimensional space.

The rows of V^T contain the elements of the *right singular eigenvectors* $\mathbf{v_k}$, $\{\mathbf{v_k}\}$ form an orthonormal basis for time delays.

S is an $n \times n$ diagonal matrix with nonzero elements on the diagonal, called the *singular values*, or eigenvalues. By convention, the ordering of the singular eigenvectors is determined by high-to-low sorting of eigenvalues, with the highest eigenvalue in the upper left index of the S matrix. For a square symmetric matrix X, SVD is a diagonalization process, or solution of the eigenvalue problem for X. In Fig. 3.1 it has been shown a graphical depiction of the SVD of a matrix X.

To obtain the SVD, calculate V^T and S by diagonalizing $X^TX = VS^2V^T$, and $U = XVS^{-1}$ using the Gram-Schmidt orthogonalization process. SVD is calculated with MATLAB® . The code is shown in Appendix B.1.

We can define the *coordinate matrix*

$$M = SV^T \tag{3.3}$$

so that $X = UM$. This is a useful way to reconstruct every experimental trace $\mathbf{a_j}$ as

$$\mathbf{a_j} = \sum_{k=1}^{n} v_{kj} s_k \mathbf{u_k} = \sum_{k=1}^{n} m_{kj} \mathbf{u_k} \tag{3.4}$$

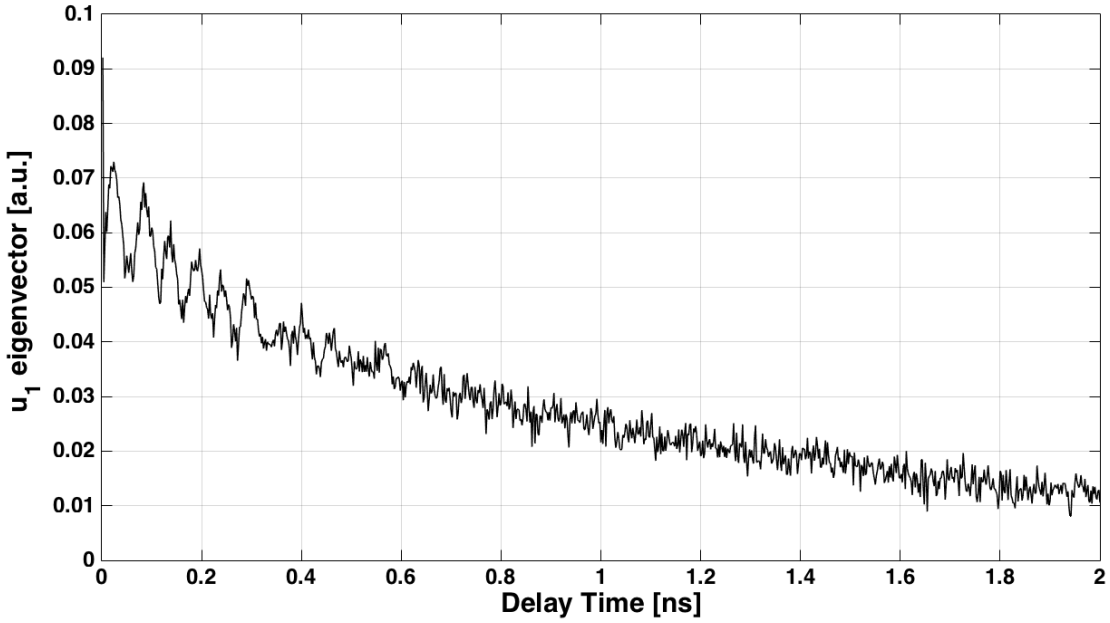

Figure 3.2: $\mathbf{u_1}$ left eigenvector versus delay time, extracted from singular value decomposition applied to nanodisks' data matrix X. The eigenvector presents the typical exponential decay with an oscillation superposed.

which is a linear combination of the eigenvectors $\{\mathbf{u_k}\}$. The m_{jk} coefficients are the projections on this orthonormal basis[4] . The rows of M contains the coordinate of each measurements projected into the eigenvectors space.

In this work the SVD is used to reduce the dimensionality of the data, projecting the data on a reduced eigenvector basis of particular relevance. How to choose the right number of eigenvectors will be the main topic of discussion.

Once the eigenvectors set will be chosen, we will perform a fit on them and then we will compare the results with the curve fitting analysis on the individual trace.

Let's start with the analysis of the nanodisks' traces. In Figg. 3.2 - 3.3 are shown the first two eigenvectors ($\mathbf{u_1}$ and $\mathbf{u_2}$) that are been calculated with SVD, starting from nanodisks' data matrix X. The eigenvector $\mathbf{u_1}$ shows the typical exponential decay with an oscillation superposed. The eigenvector $\mathbf{u_2}$ is essentially noise. The remaining eigenvectors ($\mathbf{u_3}$ to $\mathbf{u_9}$) have

[4]Therfore, the m_{kj} can be rewritten as

$$m_{kj} =< \mathbf{a_j}|\mathbf{u_k} > . \tag{3.5}$$

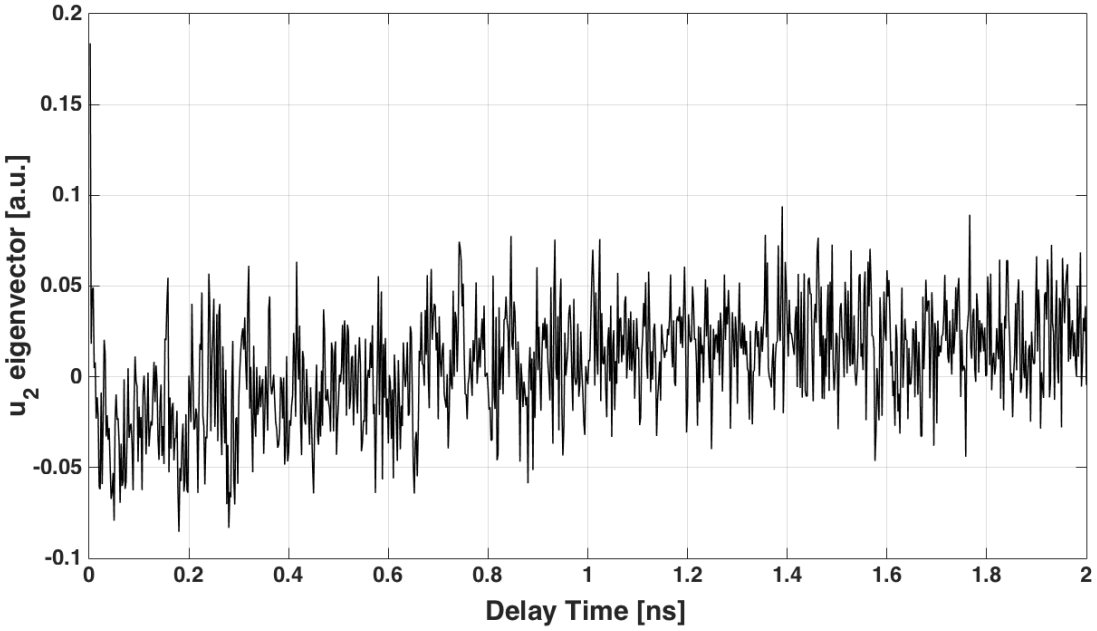

Figure 3.3: $\mathbf{u_2}$ left eigenvector versus delay time, extracted from singular value decomposition applied to nanodisks' data matrix X. The eigenvector u_2 is essentially electronic noise.

similar characteristics to the eigenvector $\mathbf{u_2}$, and are not shown.

A first way to determine if the information in the reconstruction of the experimental traces is contained only in $\mathbf{u_1}$ (as we have assumed), consists in looking at the eigenvalues s_k and at the trace projections m_{jk} on the eigenvectors basis $\{\mathbf{u_k}\}$. If the projections and the eigenvalue associated to the single eigenvector have a relative weight greater than the others, then this eigenvector alone will capture the data trend. Fig. 3.4 shows the eigenvalues and the mean of the absolute coordinates[5] for each nanodisks diameter (100 or 90 nm) and for each eigenvector. Observing Fig. 3.4, we can note that the first eigenvalue s_1 and the first projection $\overline{M}_1$ are dominant with respect to the others for both diameters. This is a remarkable result, because it

[5]For example, $\overline{M}_k$ for 90 nm nanodisk traces has been calculated as

$$\overline{M}_k = \frac{1}{5}\sum_{j=1}^{5} |m_{kj}|.$$

$\overline{M}_k$ for 100 nm nanodisk traces has been calculated as

$$\overline{M}_k = \frac{1}{4}\sum_{j=6}^{9} |m_{kj}|.$$

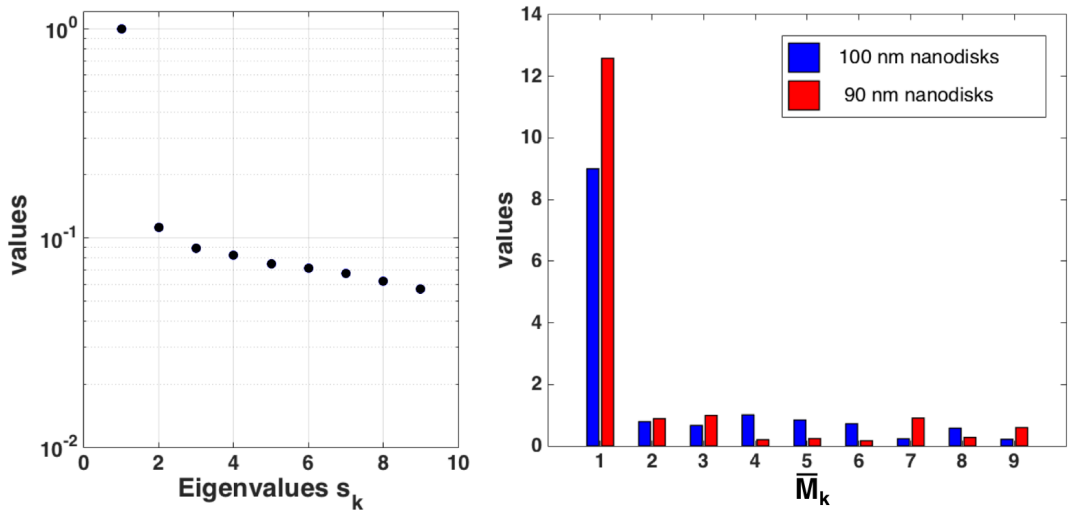

Figure 3.4: a) Eigenvalues s_k in semilogarithmic scale calculated with SVD. b) Histogram of the mean of the absolute value of the coordinates. The red bars represent the average coordinates for 90 nm nanodisks traces. The blue ones represent the average coordinates for 100 nm nanodisks traces.

confirms the initial observations.

As we have said previously, we can reduce the data dimensions by projecting the original data into a subspace spanned by the two eigenvectors with the highest eigenvalues, visualizing these coordinates as points in a scatter plot (Fig. 3.5). In this case two clusters are evidenced, each composed of points corresponding to the same nanodisk's diameter. Therefore such a kind of analysis allows us to distinguish one nanodisk's size from the other, discriminating objects whose diameter of about a hundred nanometers differs by a ten percent.

Shannon entropy

The second way that we have used to estabilish how many eigenvectors are needed to represent the data accurately, is to calculate the *Shannon entropy*[6], or information entropy. In physics, the word entropy has important implications as the amount of "randomness" of a system. In our case, we would like to find a useful tool to measure the information content of our experimental data.

[6]Shannon entropy was introduced by Claude E. Shannon in his 1948 paper "A Mathematical Theory of Communication"[14]

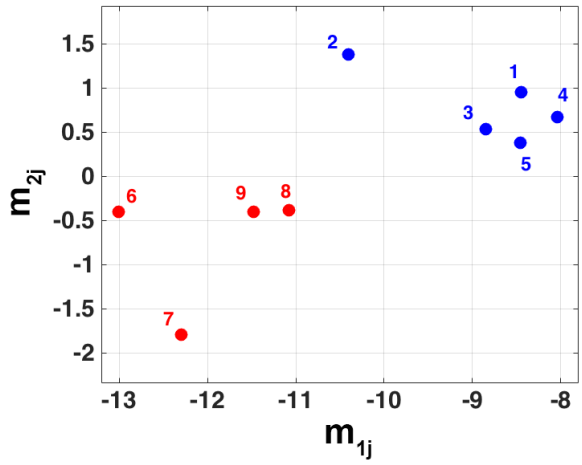

Figure 3.5: In this scatter plot each point represents the coordinates (m_{1j}, m_{2j}) of a specific trace in the space spanned by the first two eigenvectors (i.e with the highest eigenvalues). The color code and the numeration is the same of Fig. 2.13. Note that projections from disks of same diameter are grouped in clusters.

We define the *Shannon entropy* of our data set as[13]

$$0 \leq H(X) = \frac{-1}{\log(n)} \sum_{k=1}^{n} p_k \log(p_k) \leq 1, \tag{3.6}$$

where

$$p_k = \frac{{s_k}^2}{\sum_{k=1}^{n} {s_k}^2}, \tag{3.7}$$

indicates the relative significance of the kth eigenvector $\mathbf{u_k}$ in terms of fraction of the overall expression that they capture. Therefore, the equation 3.6 measures the complexity of the data from the distribution of the overall expression between the different eigenvectors, where $H(X) = 0$ corresponds to an ordered and redundant dataset in which all information is captured by a single eigenvector, and $H(X) = 1$ corresponds to a disordered and random dataset where all eigenvectors $\{\mathbf{u_k}\}$ are equally expressed.

We have calculated $H(X)$ for 100 and 90 nm nanodisks, and we have obtained $H(X) = 0.1262$ for 100 nm disks and $H(X) = 0.0593$ for 90 nm. This is an important result. Given that for both samples the entropy is close to 0, we can conclude that each experimental trace contains for both diameters the same amount of information. For this reason it is sufficient only one eigenvector to represent each group of measurements.

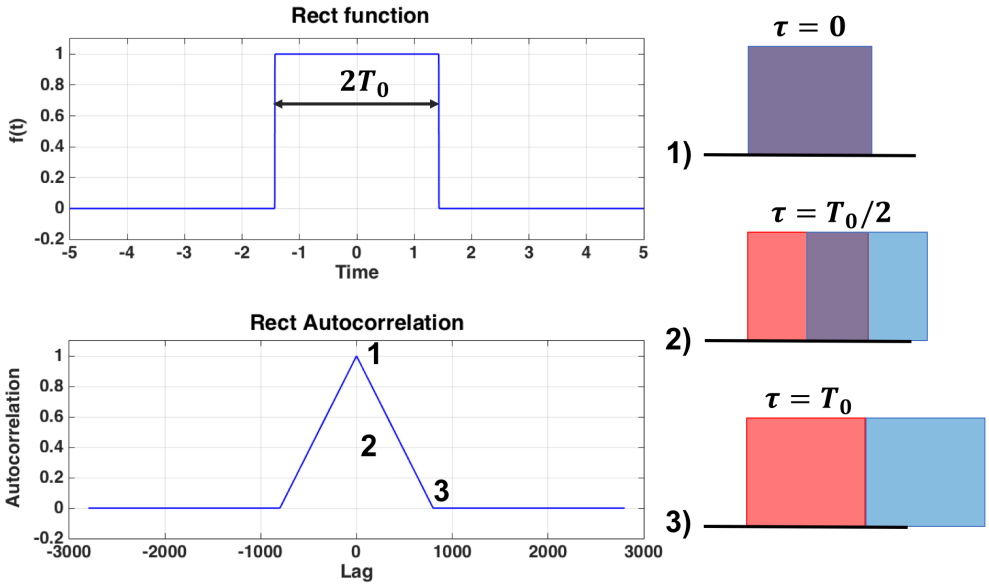

Figure 3.6: Rect function autocorrelation versus lag. 1) If $\tau = 0$ the autocorrelation function $R_{xx}(0)$ is equal to 1, because $rect(t) = rect(t + 0)$. 2) If $\tau = T_0/2$, $R_{xx}(T_0/2) = 1/2$ because the rectangles are overlapped for half and 3) for $\tau = T_0$ the rectangles are no longer superimposed and $R_{xx}(T) = 0$

Eigenvectors autocorrelation

To determine the randomness of our eigenvectors we have performed an autocorrelation. In fact, the white noise is completely decorrelated. As a starting point, we note that the autocorrelation function of a random signal describes the general dependence of the values of the signal at time t on the values of the same signal at another time $t + \tau$.

Considering a signal $f(t)$ (i.e. continuous-time), its autocorrelation function is written as:

$$R_{xx}(\tau) = \lim_{T\to\infty} \frac{1}{2T} \int_{-T}^{T} f(t)f(t+\tau)dt \tag{3.8}$$

where T is the period of observation and τ is the lag. Usually one plots the autocorrelation $R_{xx}(\tau)$ as a function of the lag τ.

When computed, the resulting number can range from +1 to -1. An autocorrelation of +1 represents perfect positive correlation and for non-periodic signal it is possible only when $\tau = 0$, while a value of -1 represents perfect negative correlation.

As an example, consider the *rect function*, equal to 1 if $-T_0 \leq t \leq +T_0$, and 0 otherwise.

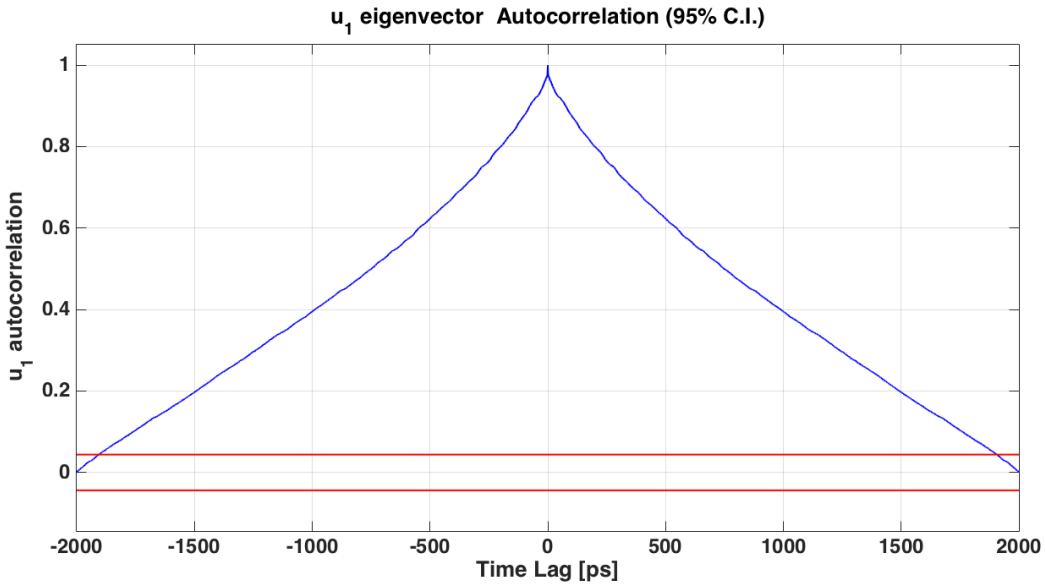

Figure 3.7: The blu line represents the autocorrelation of eigenvector $\mathbf{u_1}$ versus lag. In red the 95%-confidence bounds for a white noise autocorrelation. The autocorrelation values clearly exceed the 95 %-confidence bounds then the eigenvector $\mathbf{u_1}$ contains a signal.

As shown in Fig. 3.6 when $\tau = 0$ the autocorrelation function $R_{xx}(0)$ is equal to 1, because $\text{rect}(t) = \text{rect}(t+0)$ (1). When $\tau = T_0/2$, $R_{xx}(T_0/2) = 1/2$ because the rectangles are overlapped for half (2). At the end (3), when $\tau = T_0$ the rectangles are no longer superimposed and $R_{xx}(T_0) = 0$.

If the signal is discrete, like in our case, we have

$$R_{xx}(m) = \frac{1}{N} \sum_{n=1}^{N-m+1} f(n) f(n+m-1) \tag{3.9}$$

where m is the discrete lag.

We have applied the autocorrelation function to our SVD eigenvectors. Figg. 3.7 - 3.8 show the autocorrelations of eigenvectors $\mathbf{u_1}$ and $\mathbf{u_2}$ obtained from SVD applied to the 100 nm nanodisk traces. Similar results are been obtained with disks of 90 nm. Observing the eigenvector $\mathbf{u_1}$, we can infer that it is completely autocorrelated. This is an obvious conclusion, since it recalls our experimental traces. The autocorrelation values of the other eigenvectors (included $\mathbf{u_2}$, see Fig. 3.8) exceed the 95%-confidence bounds for a white noise autocorrelation at many lags. The oscillation probably is a weak residual of the mechanical oscillation, shown in

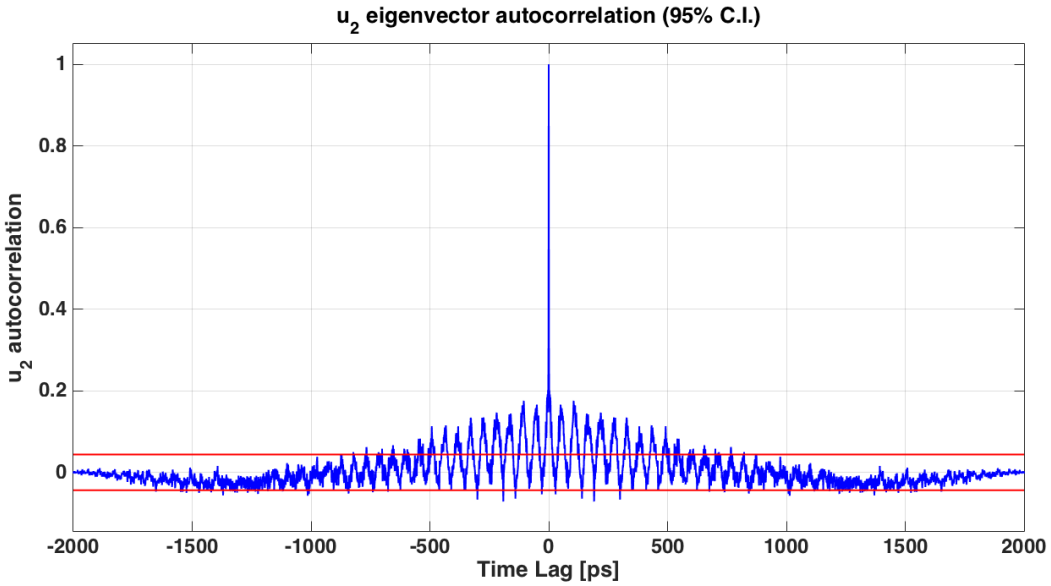

Figure 3.8: The blu line represents the autocorrelation of eigenvector $\mathbf{u_2}$ versus lag. In red the 95%-confidence bounds for a white noise autocorrelation. The autocorrelation values exceed the 95%-confidence bounds for a white noise autocorrelation at many lags. This weak oscillation probably is an high-frequency electronic noise.

Fig. 3.2.

After this final analysis we can conclude that the first eigenvector $\mathbf{u_1}$ contains all the information interesting us.

Eigenvectors analysis and curve fitting

We consider the eigenvectors $\mathbf{u_1}$ for 100 and 90 nanometers disks. Observing the curve in Fig 3.2, it is possible to recognize the two main dynamics to study: the exponential decay due to the thermal dissipation between the nanodisk and the bulk (nanosecond time scale) and the mechanical oscillation of the disk, characterized by a period of about tens of ps.

Thermal analysis

To extrapolate the time scales of the the thermal dynamics involved, we fit the eigenvector $\mathbf{u_1}$ using a linear combination of three exponential:

$$f(t) = A \cdot \exp(-t/\tau_1) + B \cdot \exp(-t/\tau_2) + C \cdot \exp(t/\tau_3)$$

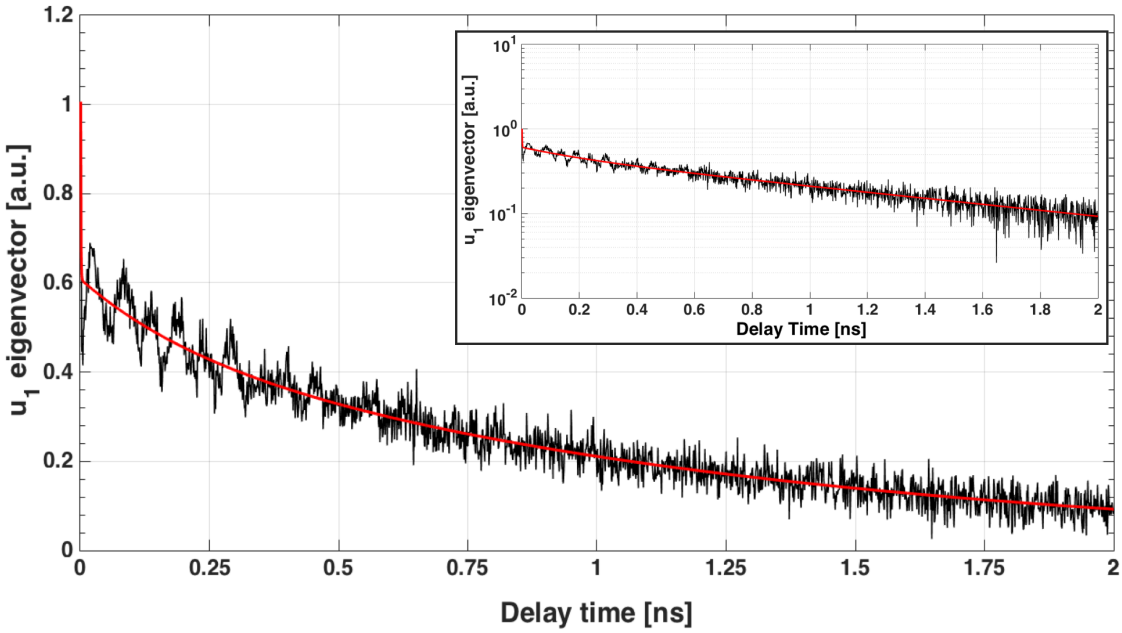

Figure 3.9: The black line represents $\mathbf{u_1}$ eigenvector versus delay time. In red the three exponential fit function. Inset: The same curves in semi-log scale.

Fig. 3.9 reports the eigenvector $\mathbf{u_1}$ and the fit function. The decay times with the 95% confidence bound for the 90 nm disk are: τ_1=556 fs (356 , 1270), τ_2 = 212 ps (166, 292), τ_3 = 1.22 ns (1.17, 1.29). For the 100 nm disk are: τ_1=1090 fs (929 , 1310), τ_2 = 166 ps (141, 204), τ_3 = 1.78 ns (1.70, 1.87). The complete coefficients tables (with the corresponding confidence interval) are reported in Table C.2 and Table C.1 in Appendix C. For both diameter the value τ_1 is confrontable with the e-ph coupling time, τ_2 and τ_3 are comparable with thermal relaxation between the nanodisk and the bulk[7]

We are now interested in the analysis of fit coefficients, amplitude and rate of decay, one for each exponential, for both the nanodisk's diameter, 90 and 100 nm. In particular, we want to confront the coefficients obtained from the analysis of the SVD eigenvectors with those obtained from the fit of the individual experimental traces, that are shown in Fig 2.13.

Plotting the rates of decay and the amplitudes as represented in Figg. 3.10 - 3.11, we observe a clear trend to cluster around a certain values, that are the values obtained from the fitting of

[7]An estimate for the thermal relaxation time between the disk and the substrate is given in the Ronchi's Bachelor thesis[12].

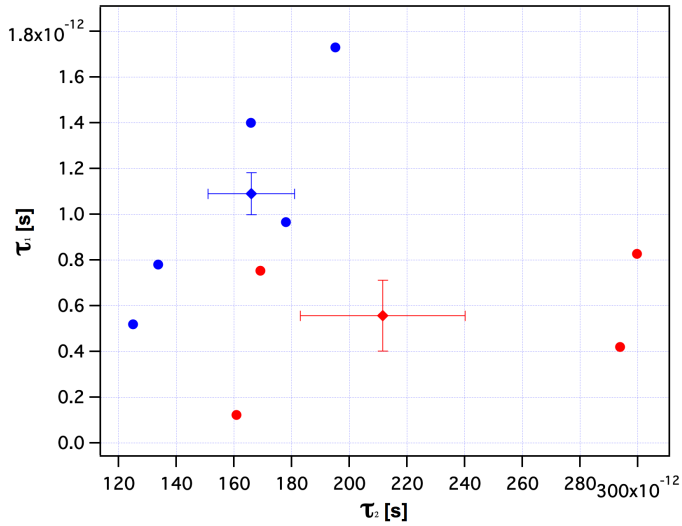

(a) Absolute values of τ_1 vs τ_2

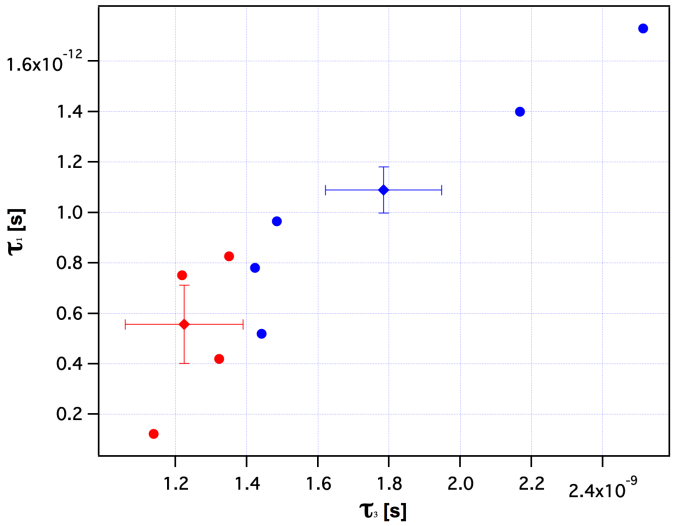

(b) Absolute values of τ_1 vs τ_3

Figure 3.10: Red markers represent the curve fitting values related to 90 nm single traces, while blue dots the ones linked to the 100 nm traces. The square markers represent the values (with the corresponding error bars) obtained from the fitting of SVD eigenvectors.

SVD eigenvectors. This confirms that the SVD eigenvectors represent all the measurements of the data matrix X.

As we can see, to each value of the SVD eigenvector curve fit are associated the corresponding

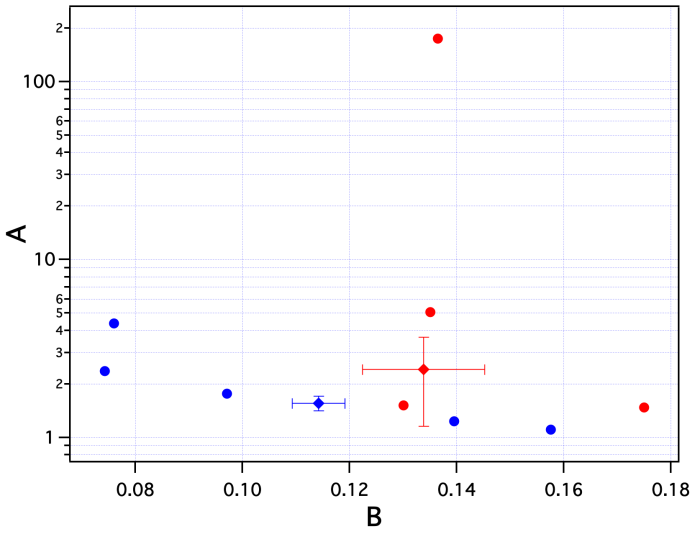

(a) Absolute values of A vs B in semilog scale.

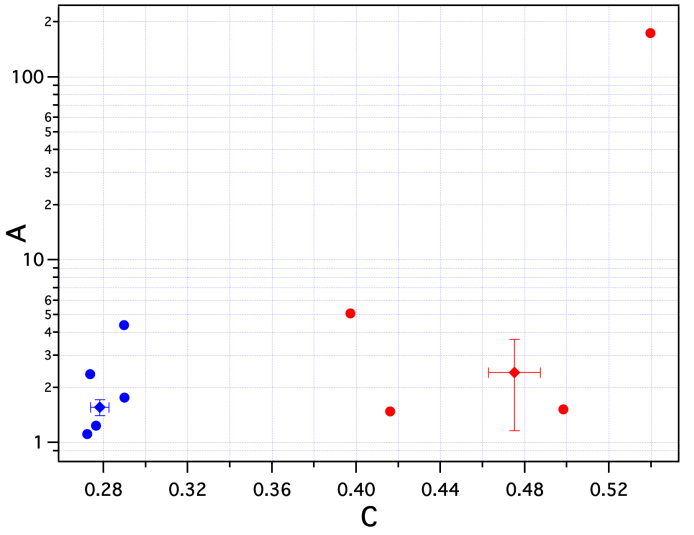

(b) Absolute values of A vs C in semilog scale.

Figure 3.11: Red markers represent the curve fitting values related to 90 nm single traces, while blue dots the ones linked to the 100 nm traces. The square markers represent the values (with the corresponding error bars) obtained from the fitting of SVD eigenvectors.

error bars, evaluated from the standard deviation of the measure itself. This uncertainty results from the process of statistical analysis computed by MATLAB® . It is interesting to note that the scatter of the points is much bigger than the error on the single SVD value. This means that

the SVD analysis is a powerful tool to reduce systematic errors. In general, this kind of error are related to the variation of some experimental variable, like temperature, humidity or laser fluctuations.

Mechanical analysis

The mechanical oscillations of the disk shown in Fig. 3.2 can be described by the theory of linear elasticity. An ideal elastic material deforms in proportion to the applied force and recovers its original size and its state (no damage) when the load is removed (Hooke's law).

An elastic wave is a mechanical perturbation that propagates through the material causing oscillations of the particles that constitute it with respect to their equilibrium position. The real materials differ from the ideal model in different ways but in particular for the dissipation mechanisms.

In our system an intense pump pulse impulsively delivers to the disk an energy density dU. From this moment, the physics is well represented by the following three steps. In the first step, the ultra-short laser pulse heats the electronic gas of the nanodisk. In the second step, the electronic gas delivers energy to and thermalizes with the lattice. In the last step, the local increase of temperature dT is responsible for an impulsive expansion of the lattice through the thermal expansion coefficient α. At this point, (A) the nanodisk thermalizes with the substrate (B) the impulsive expansion of the disk, that is coupled mechanically with the substrate, excites a displacement field $\mathbf{u}(\mathbf{r}, t_0)$.

The displacement field, defined as

$$\mathbf{u}(\mathbf{r}, t) = \mathbf{r}(t) - \mathbf{r}(t_0)$$

(where $\mathbf{r}(t)$ and $\mathbf{r}(t_0)$ are respectively the position vectors at time t and t_0) is the solution of the Navier equation

$$(\lambda + \mu) \text{ grad div } \mathbf{u} + \mu \nabla^2 \mathbf{u} = \rho \frac{\partial^2 \mathbf{u}}{\partial t^2} \tag{3.10}$$

where λ and μ are the Lamé constants of the material forming the object, and ρ is its material density. The initial conditions for the dynamics are defined by the fields $\mathbf{u}(\mathbf{r}, t_0)$ and $\dot{\mathbf{u}}(\mathbf{r}, t_0)$. The eigenmodes correspond to harmonic solutions of Eq. 3.10:

$$\mathbf{u}(\mathbf{r}, t) \;=\; \mathbf{u}(\mathbf{r}) \exp(i\tilde{\omega} t) \tag{3.11}$$

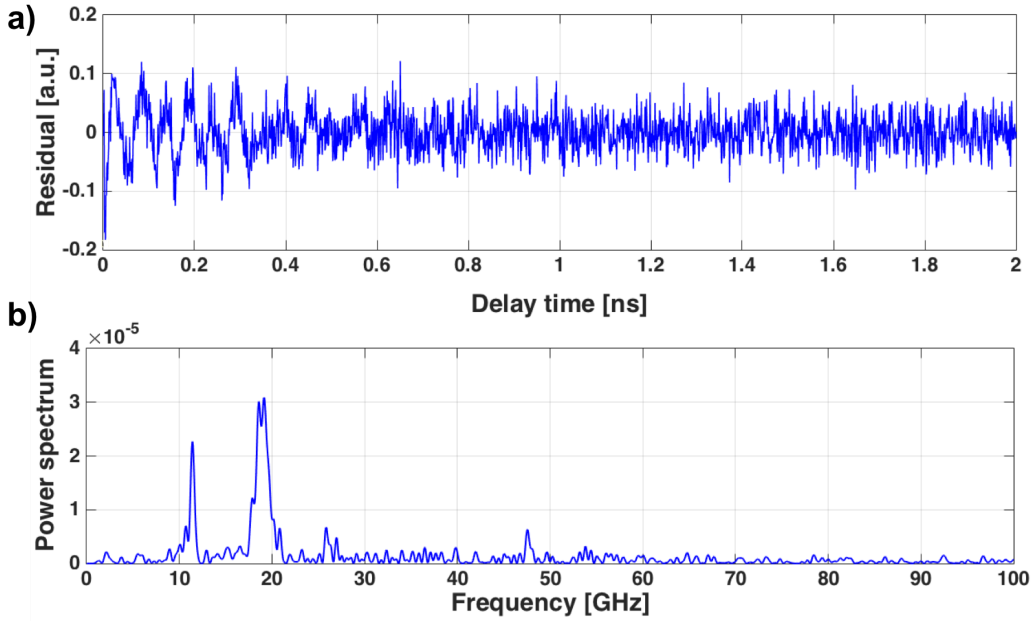

Figure 3.12: (a) shows the residues of eigenvector $\mathbf{u_1}$ versus delay time obtained from the fit represented in Fig. 3.9. In (b) we can see the power spectrum of residual in (a). It is interesting to observe two peaks, corresponding to the frequency of the two oscillator in (a). These frequencies are comparable with those obtained in Ronchi's bachelor thesis[12].

where the vibrational frequencies $\tilde{\omega}$ are real or complex valued in the case of free and substrate-coupled nanodisk, respectively. In the coupled case, their imaginary part reflects damping of the vibration mode by the transfer of mechanical energy to the lattice.

To find the frequencies of the disk's mechanical oscillations, we compute a *Discrete Fourier Transform* (DFT) of the residues of the triple-exponential fit of the eigenvector $\mathbf{u_1}$. The Fourier transform relates the function's time domain to the function's frequency domain and it is defined as

$$\hat{f}(\mathbf{k}) = \int_{-\infty}^{+\infty} f(\mathbf{x}) e^{-2\pi i \mathbf{k}\cdot\mathbf{x}} d\mathbf{x} \tag{3.12}$$

$$\hat{f}(\mathbf{x}) = \int_{-\infty}^{+\infty} f(\mathbf{k}) e^{2\pi i \mathbf{k}\cdot\mathbf{x}} d\mathbf{k} \tag{3.13}$$

The discrete versions of Eqs. 3.12 and 3.13, DFT and iDFT, employ an algorithm called Fast Fourier Transform (FFT), that computes the discrete summation

$$F_k = \sum_{n=1}^{N} f_n e^{-2\pi i (k-1)(n-1)/N}, \quad 1 \leq k \leq N \tag{3.14}$$

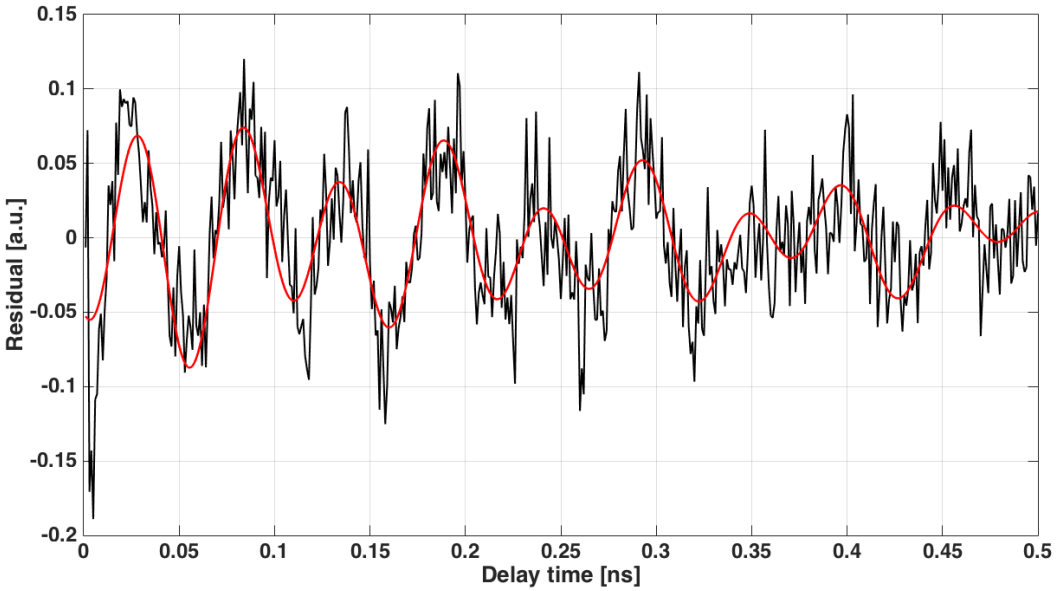

Figure 3.13: In black: the residual of eigenvector $\mathbf{u_1}$ versus delay time up to 500 *ps*, obtained from the fit represented in Fig. 3.9. In red: fit curve obtained with the linear combination of two damped sines.

F_k are the DFT coefficients of a signal f_n (with index $n = 1, 2, \ldots, N$). The inverse transform is given by

$$f_n = \frac{1}{N} \sum_{n=1}^{N} F_k e^{-2\pi i(k-1)(n-1)/N}, \quad 1 \leq k \leq N \tag{3.15}$$

Our signal is formed by a discrete number of points N, so the frequency resolution of DFT is

$$\Delta\nu_{DFT} = \frac{1}{N \cdot \Delta t} = \frac{1}{t_{max}} \tag{3.16}$$

where Δt and t_{max} are the resolution and the temporal window of the measurements, respectively. An example of residues and the relative power spectrum is shown in Fig. 3.12. From the frequency values of DFT, it is possible to estimate the period of these mechanical oscillation as the inverse of frequency. Observing the residues of eigenvector $\mathbf{u_1}$, we can see that these oscillators are damped.

To analayze in detail the mechanical oscillations we have fitting the residues of the eigenvector $\mathbf{u_1}$ with a linear combination of two damped sines (Fig. 3.13):

$$f(t) = A \exp\left(-\frac{t}{\tau_1}\right) \sin\left(\frac{2\pi}{T_1}t + \phi_1\right) + B \exp\left(-\frac{t}{\tau_2}\right) \sin\left(\frac{2\pi}{T_2}t + \phi_2\right) \tag{3.17}$$

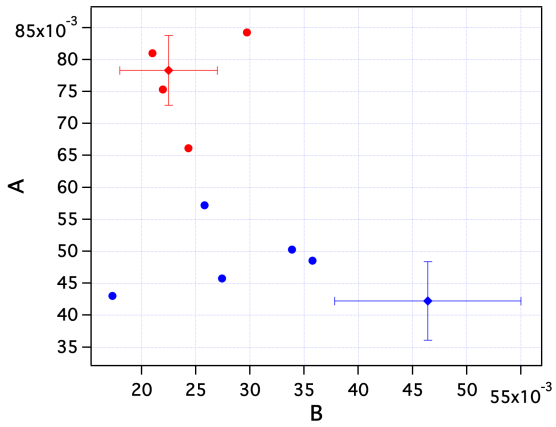

(a) A vs B

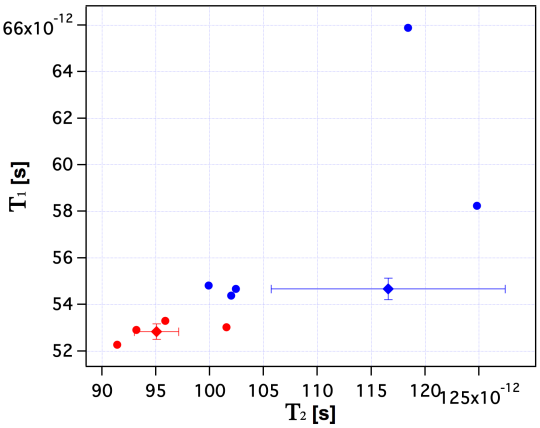

(b) T_1 vs T_2

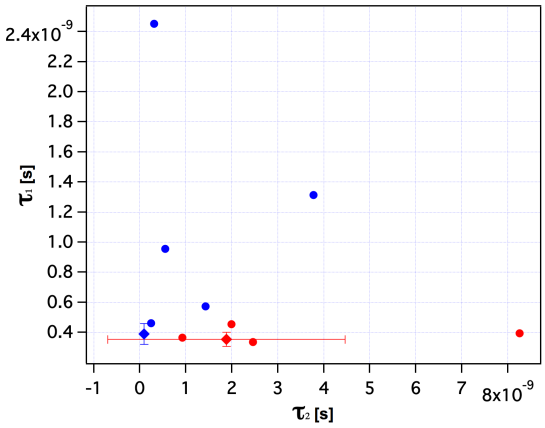

(c) τ_1 vs τ_2

Figure 3.14: Amplitude A, temporal period T and rate of decay τ for the first oscillator versus same coefficients for the second one for each experimental trace. Red markers represent the values corresponding to the 100 nm gold nanodisks, while blue dots the ones corresponding to the 90 nm.The square markers represent the values (with the corresponding error bars) obtained from the fitting of residual of SVD eigenvectors.

As for the thermal analysis, we are interested in fit coefficients[8], amplitude A, temporal period T and rate of decay τ, for each oscillators of both nanodisk's diameter. Plotting the fit coefficients of each experimental trace in a scatter graph and confronting these with the SVD's one, we

[8]The complete coefficients tables (with the corresponding confidence interval) are reported in Table C.3 and Table C.4 (see Appendix C).

obtain the graphs in Fig. 3.14.

Looking at the graphs, we observe that there is a trend to cluster, therefore such a kind of analysis allows us to distinguish one sample from the other. With respect to the thermal part, the fit coefficients of the SVD only partly capture the global trend the measurements, in particular, the amplitudes A and decays τ. This is easily explained because the amplitude and the dumping of the oscillations are partly lost in the singular value decomposition.

If we analyze the periods T, the SVD value represents an average of the values for the single measures. These periods are comparable with both the frequencies extracted from the DFT.

We conclude that the study of the first eigenvectors extracted from the SVD allows us to analyze the thermomechanical dynamic of this nanosystem.

3.1.2 Hierarchical cluster analysis

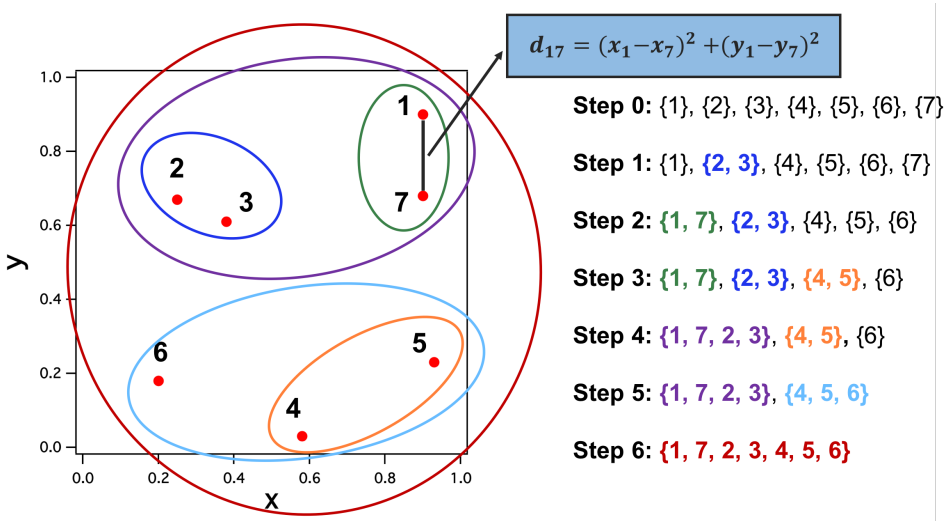

Figure 3.15: Graphical representation of an agglomerative hierarchical clustering algorithm. At the step 0, all clusters are singletons (clusters containing a single point). At the end (step 6), there is only one big cluster with seven elements. At each step the numerical solver finds the pair of clusters that leads to minimum increase in total within-cluster variance after merging. This increase is a weighted squared Euclidean distance between cluster centers.

In this section, we aggregate the experimental traces contained in the column of matrix X in a dendrogram, using a hierarchical clustering principle. A dendrogram is a tree diagram frequently used to illustrate the arrangement of the clusters produced by hierarchical clustering obtained with algorithms known as linkage rules.

In this work we have used a linkage rule known as "Ward minimum variance method". This is an agglomerative method that clusters data with the criterion to minimize the total within-cluster variance once an appropriate metric has been defined to measure the distance among the experimental trace.

An example of how the algorithm works is shown in Fig. 3.15. At each step the numerical solver finds the pair of clusters C_i and C_j that leads to minimum increase in total within-cluster variance after merging. This increase is a weighted squared distance between cluster centroids. At the initial step, all clusters are singletons (clusters containing a single point). At the end, there is only one big cluster. To apply a recursive algorithm, we have to define a initial distance between individual objects. We have chosen a squared Euclidean distance, that for two generic

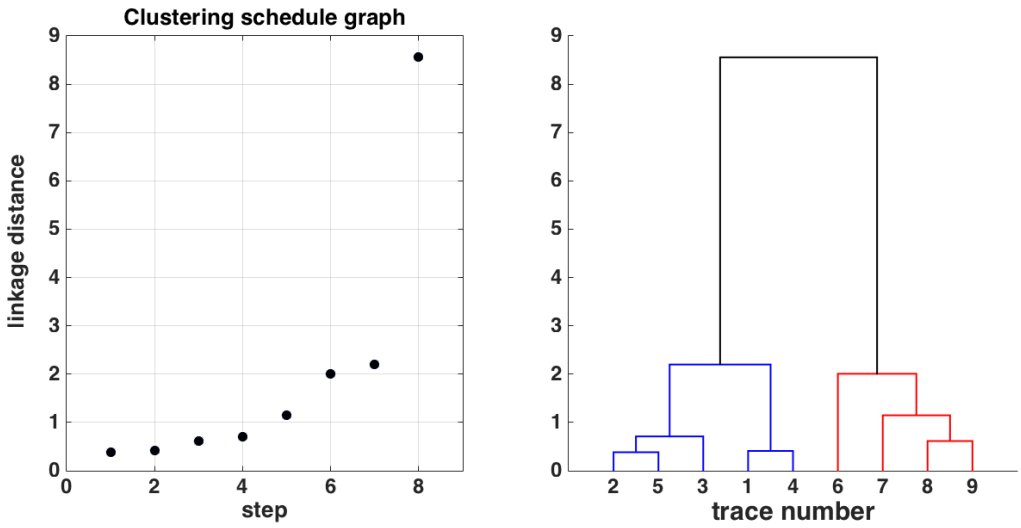

Figure 3.16: Hierarchical cluster analysis. Dendrogram obtained using the Ward's method. The vertical lengths between nodes are proportional to the linkage distance. In blue: cluster of the 100 nm gold nanodisk's measures. In red: cluster of the 90 nm gold nanodisk's measures.

points x_i, x_j is define as

$$d_{ij} = ||x_i - x_j||^2. \tag{3.18}$$

For this reason, the linkage distance, or *Ward's linkage*, will be defined as

$$d_{ij} = d(C_i, C_j) = \sqrt{\frac{2n_i n_j}{(n_i + n_j)}} ||\bar{C}_i - \bar{C}_j||^2. \tag{3.19}$$

where $\bar{C}_i$,$\bar{C}_j$ are the centroids of clusters i and j, and n_i,n_j are the number of elements in clusters i and j.

The results of hierarchical clustering are presented in the dendrogram shown in Fig. 3.16[9]. The data group in two distinct clusters, each associated to one nanodisk's diameter. Thus, this algorithm allows us to reveal the internal similarities in our data, in particular, it differentiate objects in the 100 nm range differing in dimension by less than 10 %. In the next sections, we will try to use this powerful tool to recognize the different dilution properties in the nanospheres' experimental traces.

[9]The MATLAB® code used to perform this analysis is presented in Appendix B.2.

3.2 Gold nanospheres

3.2.1 Singular Value Decomposition

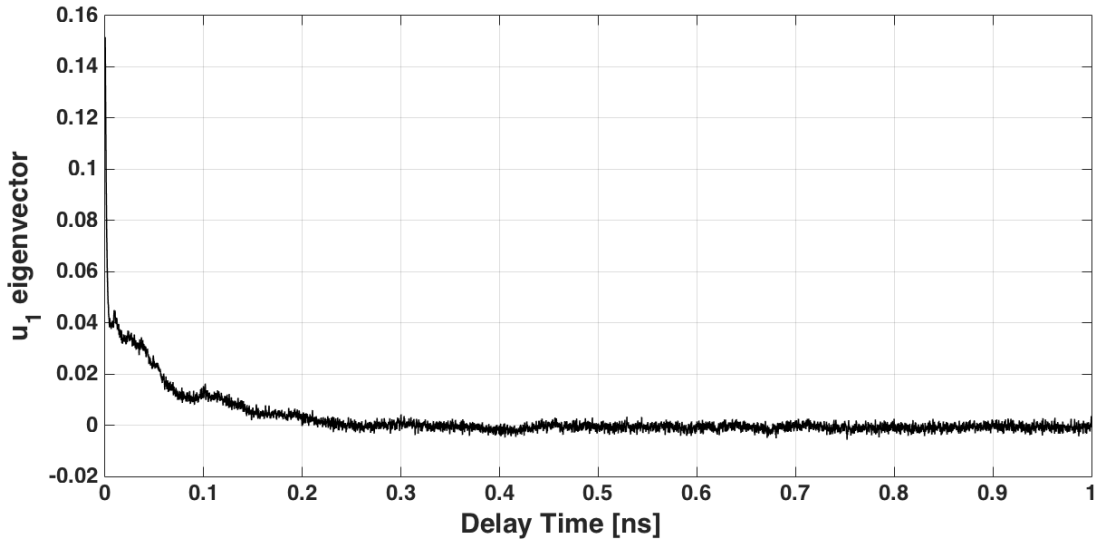

Figure 3.17: $\mathbf{u_1}$ left eigenvector versus delay time up to 1 ns, extracted from singular value decomposition applied to nanospheres' data matrix X. The eigenvector presents the typical exponential decay with a weak oscillation superposed.

Now we analyze the nanospheres' traces. In Figg. 3.17 - 3.18 are shown the first two eigenvectors ($\mathbf{u_1}$ and $\mathbf{u_2}$) calculated with SVD, starting from nanospheres' data matrix X. In this case the matrix X has 35000 rows and 9 columns.

As we can see the eigenvector $\mathbf{u_1}$ presents the typical exponential decay. Unlike the nanodisks, the mechanical oscillations are less evident. These oscillations are also present in the second eigenvector $\mathbf{u_2}$. Note that a noise of equal amplitude is superposed to this oscillation. The remaining eigenvectors ($\mathbf{u_3}$ to $\mathbf{u_9}$) have similar characteristics to the eigenvector $\mathbf{u_2}$, and are not shown.

As for nanodisks, we examine the eigenvalues s_k and the trace projections m_{jk} on the eigenvectors basis $\{\mathbf{u_k}\}$. If the projections and the eigenvalue associated to the single eigenvector have a relative weight greater than the others, then the corresponding eigenvector will be more important than others in the data reconstruction.

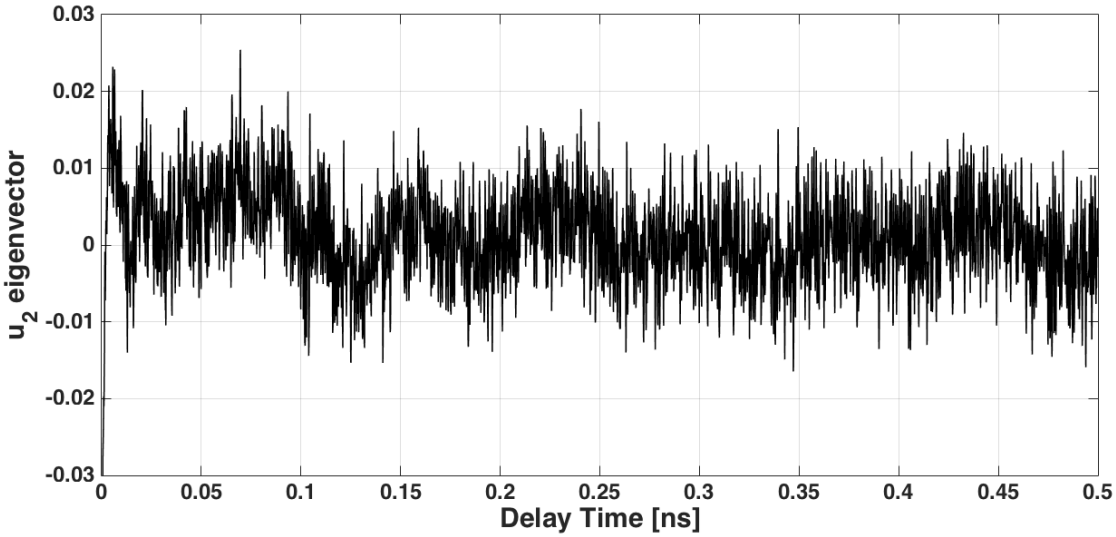

Figure 3.18: $\mathbf{u_2}$ left eigenvector versus delay time, extracted from singular value decomposition applied to nanospheres' data matrix X. The eigenvector $\mathbf{u_2}$ presents an oscillation with a noise of same amplitude superposed.

In Fig. 3.19 we observe that, for the sample A, the projections of each experimental trace follow a similar trend. This also applies to the sample E. Therefore, we are able to identify each sample (i.e. the dilutions of nanoparticles and antibody) studying the trend of these projections. Given that the traces from each sample have a similar trend, we mediate them to highlight the two trends. Fig. 3.20 shows eigenvalues and the mean of the absolute value of the coordinates m_{ij} for each nanospheres' sample and for each eigenvector[10].

We consider two samples with different concentration of nanoparticles and antibody. The sample A (blue points) has nanoparticles diluted 1:10 with respect to the manufacture's dilution and 0.1 mg/ml antibody. The sample E (red points) has nanoparticles undiluted with respect to the

[10]For example, $\overline{M}_k$ for sample E traces has been calculated as

$$\overline{M}_k = \frac{1}{6}\sum_{j=1}^{6} |m_{kj}|.$$

$\overline{M}_k$ for sample A traces has been calculated as

$$\overline{M}_k = \frac{1}{3}\sum_{j=7}^{9} |m_{kj}|.$$

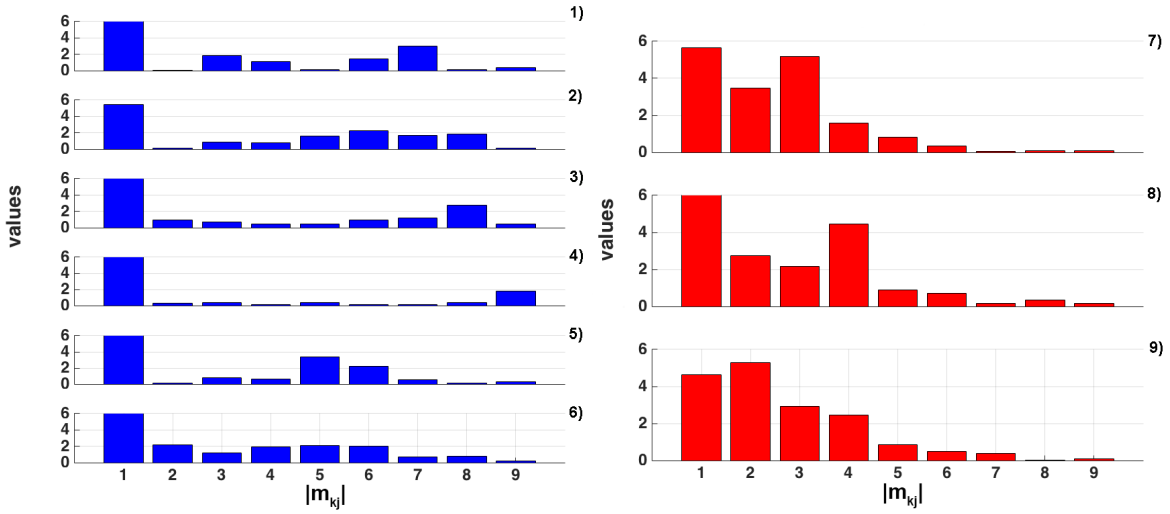

(a) Sample E (b) Sample A

Figure 3.19: a) Histogram of the absolute value of the coordinates for sample E. b) Histogram of the absolute value of the coordinates for sample A.

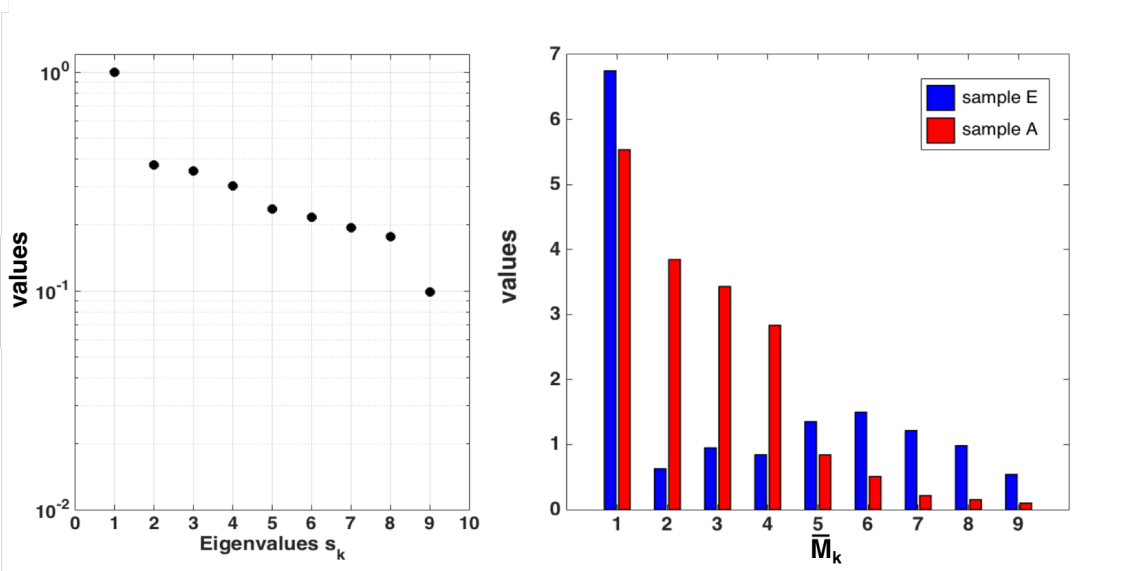

Figure 3.20: a) Eigenvalues s_k in semilogarithmic scale calculated with SVD. b) Histogram of the mean of the absolute value of the coordinates. The red bars represent the average coordinates for sample A traces. The blue ones represent the average coordinates for sample E traces.

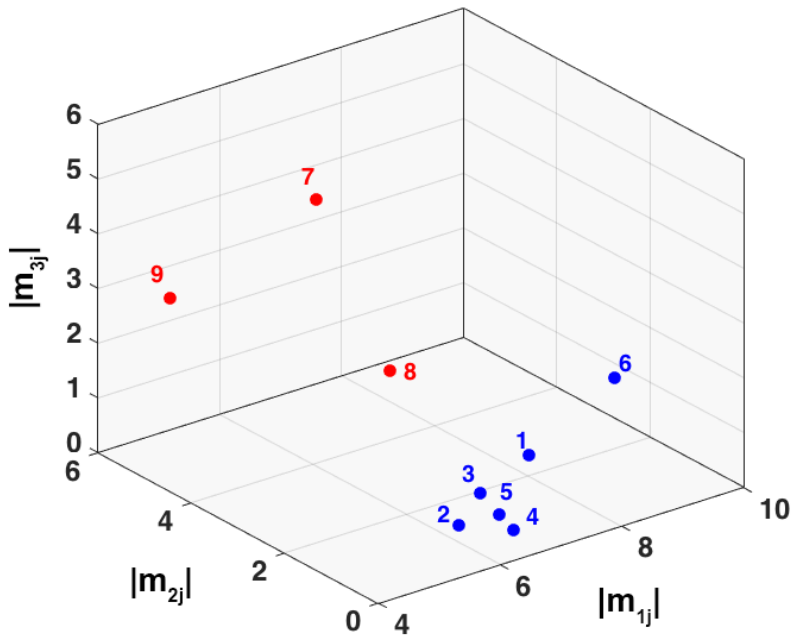

Figure 3.21: In this 3D scatter plot each point represents the absolute value of the coordinates ($|m_{1j}|$, $|m_{2j}|$, $|m_{3j}|$) for a specific trace in the space spanned by the first three eigenvectors (i.e with the highest eigenvalues). The color code and the numeration is the same of Fig. 2.14. Note that projections from same samples (A and E) are grouped in clusters.

manufacture's dilution and 1 mg/ml antibody.

Observing Fig. 3.20, we note that, for sample E, the first eigenvalue s_1 and the first projection $\overline{M}_1$ are dominant with respect to the others. For sample A, we have similar values for the first four projections ($\overline{M}_1$ to $\overline{M}_4$). This is an interesting result, because the first four eigenvectors have similar weight in reconstructing the traces of the sample A. Therefore, the projections on the first two eigenvectors are not sufficient as for the nanodisks. In this case, we have reduced the data dimensions by projecting the original data into a subspace spanned by the three eigenvectors with the highest eigenvalues, visualizing the absolute value of these coordinates as points in a 3D scatter plot. In Fig. 3.21, we identify two clusters, each composed of points corresponding to the same sample. This is an important result, because such kind of analysis allows us to discriminate one dilution from the other.

Note that the distance of the trace 6 from the centroid of the blue cluster is greater than the

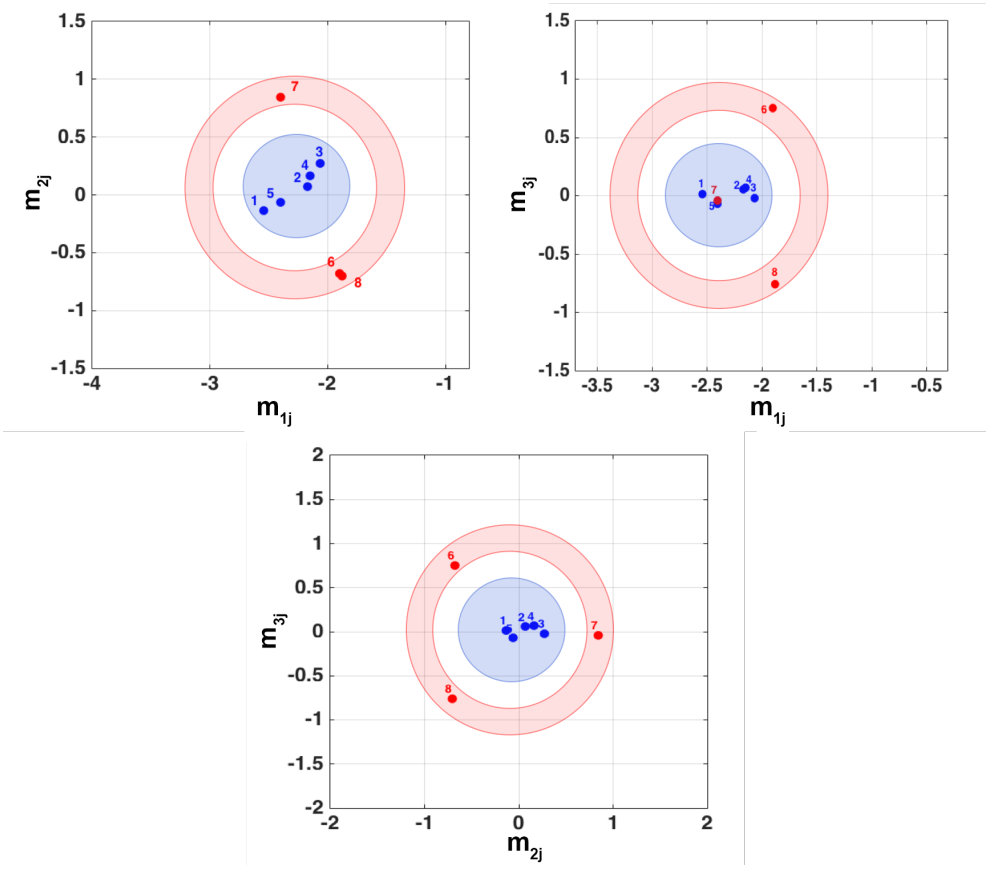

Figure 3.22: In these 2D scatter plots each point represents the value of the coordinates (m_{1j}, m_{2j}, m_{3j}) for a specific trace in the space spanned by the two eigenvectors (i.e m_{1j} vs m_{2j}, m_{1j} vs m_{3j} and m_{2j} vs m_{3j}). The color code and the numeration is the same of Fig. 2.14. Note that projections are symmetric with respect to the centroids of the clusters.

average distance of the other traces. This suggests that the measure may be not reliable. In fact, some fluctuations of the experimental conditions could be affected the measurement. The trace 6 will be removed from the subsequent analysis also in consideration of the dendrogram analysis (see below).

The choice of representing in Fig. 3.21 the absolute values of the coordinates is due to the fact that the sign of these projections identifies only a phase factor between the trace and the eigenvector on which the trace is projected. Indeed, in Fig. 3.22 we observe that the values of the coordinates (without the absolute value) are symmetric with respect to the centroids of the clusters.

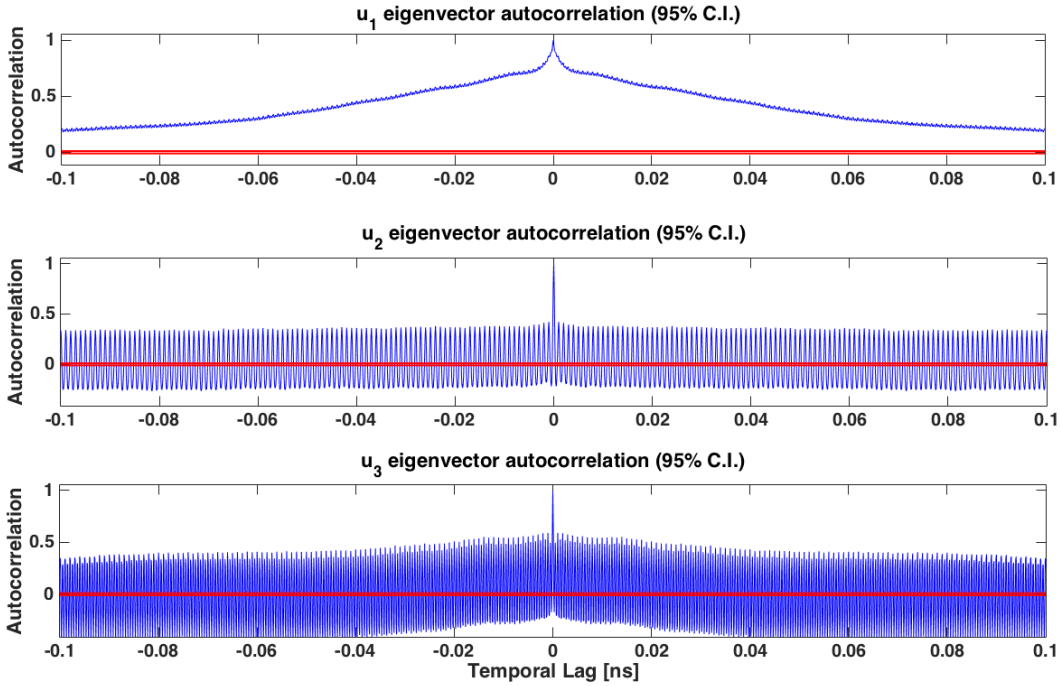

Figure 3.23: Autocorrelation of the first three eigenvectors versus temporal lag (sample E). In red the 95%-confidence bounds for a white noise autocorrelation.

Shannon Entropy

We have calculated the Shannon entropy $H(X)$ on sample A and E. We obtain $H(X) = 0.5735$ for sample A and $H(X) = 0.1846$ for sample E. With respect to the nanodisks, both these values are higher. In particular, the entropy of the sample E is comparable to the nanodisks' one. The entropy of the sample A is about five times higher. For this reason it seems to be sufficient only one eigenvector $\mathbf{u_1}$ to represent the experimental traces of the sample E. We can not say the same for the sample A, where we need more than one eigenvector.

Eigenvectors autocorrelation

To determine the randomness of our eigenvectors we have calculated the autocorrelation of the SVD eigenvectors.

Fig. 3.23 shows the autocorrelations of the first three eigenvectors obtained from SVD analysis and applied to the sample E traces. Similar results are been obtained with the sample A. Observing Fig. 3.23 we see that the $\mathbf{u_1}$ eigenvector has a high degree of autocorrelation. This is

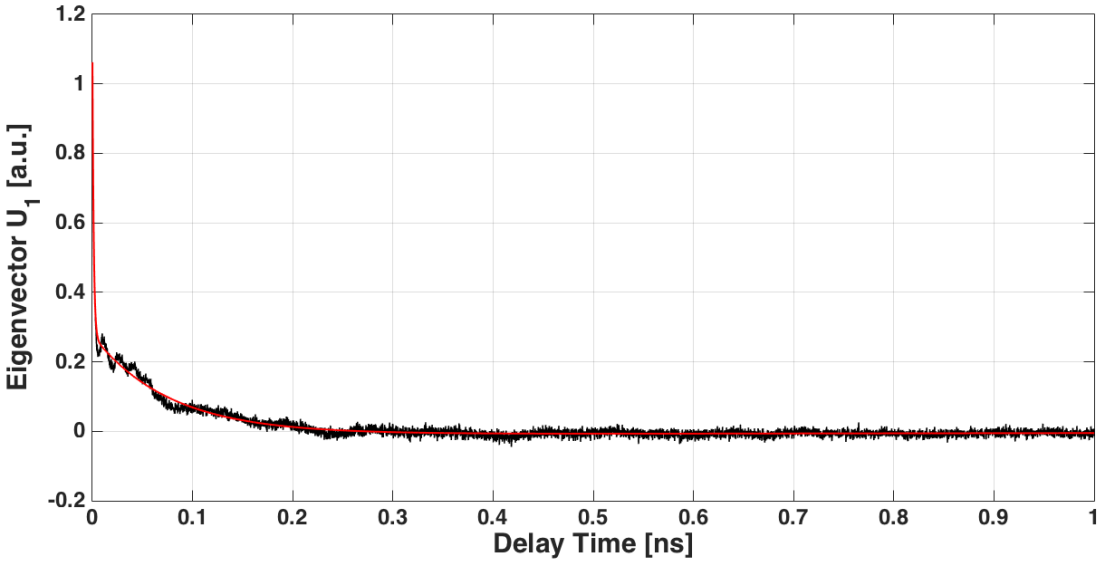

Figure 3.24: The black line represents $\mathbf{u_1}$ eigenvector versus delay time. In red the three exponential fit function.

an obvious conclusion, since the first eigenvector contains the exponential decay common to all experimental traces.

The values of the autocorrelation function for the other eigenvectors $\mathbf{u_2}$ and $\mathbf{u_3}$ periodically exceed the 95%-confidence bounds for a white noise autocorrelation. This oscillation is due to electronic noise.

After this final analysis we conclude that, for sample E, the thermomechanical dynamics is contained only in the first eigenvector $\mathbf{u_1}$. For this sample we are going to follow the same thermal and mechanical analysis shown in the previous section. For the sample A, we are going to analyze the thermal dynamics studying the eigenvector $\mathbf{u_1}$. The mechanical oscillations will be investigated evaluating the eigenvector $\mathbf{u_2}$.

Eigenvectors analysis and curve fitting

We consider the eigenvectors $\mathbf{u_1}$ and $\mathbf{u_2}$ for nanospheres' samples. Observing the curves in Figg. 3.17 - 3.18, it is possible to recognize the two main dynamics: The exponential decay due to the thermal dissipation between the nanosphere and the surrounding environment (hundred picosec-

ond - nanosecond time scale) and the mechanical oscillation of the particle, characterized by a period of tens of ps.

Thermal analysis

To extrapolate the time scales of the the thermal dynamics involved, we fit the eigenvector u_1 using a linear combination of three exponential:

$$f(t) = A \cdot \exp(-t/\tau_1) + B \cdot \exp(-t/\tau_2) + C \cdot \exp(t/\tau_3)$$

Fig. 3.24 reports the eigenvector $\mathbf{u_1}$ and the fit function. The decay times with the 95% confidence bound for sample A are: τ_1=929 fs (890, 971), $\tau_2 = 72.6$ ps (71.1, 74.3), $\tau_3 = 1.68$ ns (1.23, 2.66). For sample E we have obtained: τ_1=1250 fs (1230, 1270), $\tau_2 = 78.0$ ps (77.3, 78.7), $\tau_3 = 1.50$ ns (1.41, 1.59). The complete coefficients tables (with the corresponding confidence interval) are reported in Table C.5 and Table C.6 (see Appendix C)[11] . For both samples, the value τ_1 is similar to the e-ph coupling time, τ_2 and τ_3 are comparable with the typical time scales of the thermal relaxation between the nanoparticle and the environment.

We now analyze the fit coefficients, amplitude and rate of decay, one for each exponential, for both the nanospheres' samples. First of all, we compare the coefficients obtained from the analysis of the SVD eigenvectors with those obtained from the fit of the individual experimental traces, that are shown in Fig 2.14. In second instance, we verify if the different diluition of the nanoparticles can in some way be a discriminating factor for our measurements, in other words if more or less high concentration of particle influence the thermal dynamics of the sample.

Plotting the rates of decay and the amplitudes as represented in Figg. 3.25 - 3.26, we observe a trend to cluster around the values obtained from the fitting of SVD eigenvectors, for both samples. This confirms that the SVD eigenvectors represent on the average the overall measurements. However, there is no evidence of a connection between the amplitudes and rates of decay with the diluition of nanoparticles on the sample. The projection of the experimental traces into a sub-space spanned by the first three eigenvectors allows a more clearly identification of the two dilutions. (Fig. 3.21)

[11] These fit coefficients are comparable with those presented in Bianchetti's Bachelor thesis[15].

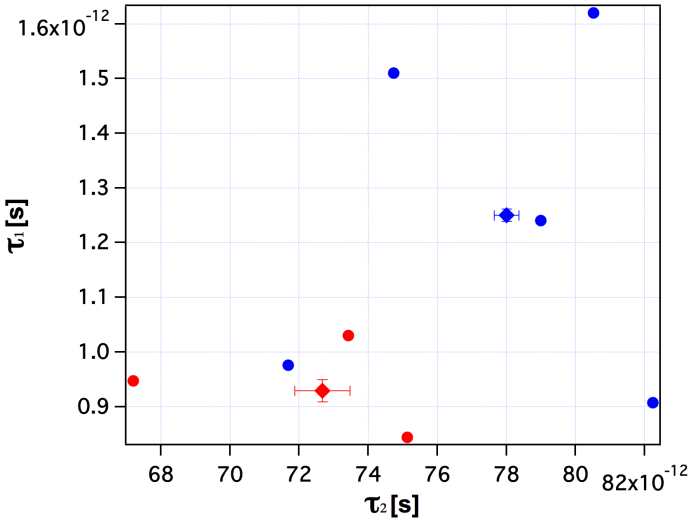

(a) Absolute values of τ_1 vs τ_2

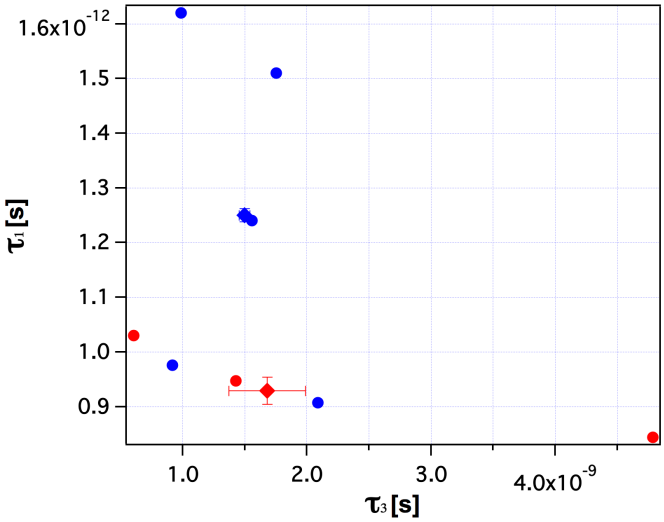

(b) Absolute values of τ_1 vs τ_3

Figure 3.25: Red markers represent the curve fitting values related to sample A traces, while blue dots the ones related to the sample E. The square markers represent the values (with the corresponding error bars) obtained from the fitting of SVD eigenvectors.

As we can see, to each value of the SVD eigenvector curve fitting are associated the corresponding error bars, evaluated from the standard deviation of the measure itself. This uncertainty results from the process of statistical analysis followed by MATLAB® . It is interesting to note

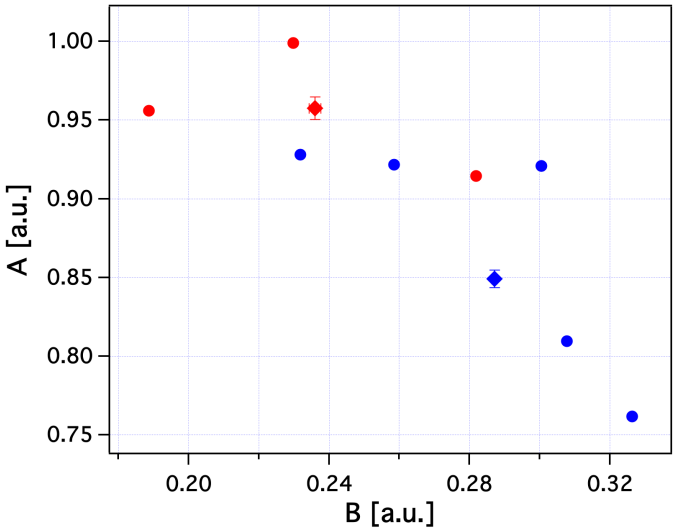

(a) Absolute values of A vs B.

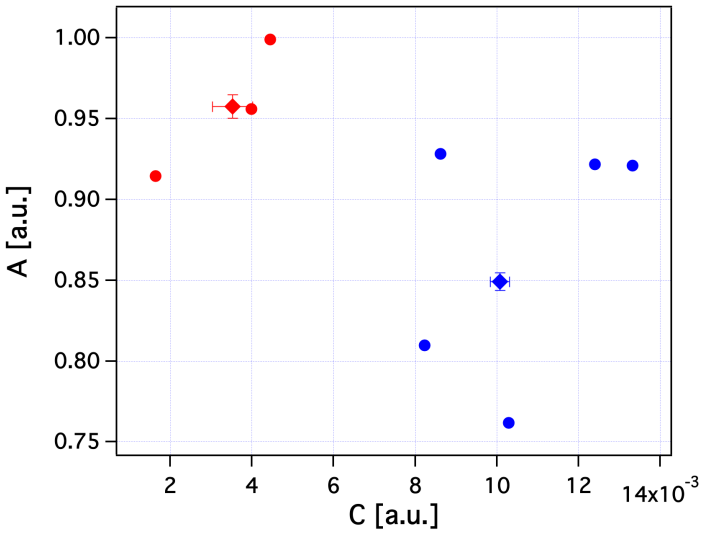

(b) Absolute values of A vs C.

Figure 3.26: Red markers represent the curve fitting values related to sample A traces, while blue dots the ones related to the sample E. The square markers represent the values (with the corresponding error bars) obtained from the fitting of SVD eigenvectors.

that the scatter of the points is much bigger than the error on the single SVD value.

This means that the SVD analysis is a powerful tool to reduce systematic errors. In general, this kind of error are related to the variation of some experimental variable, like temperature,

humidity or laser fluctuations.

Mechanical analysis

We solve numerically the Navier equation (Eq. 3.10) in the particular case of a gold nanosphere. We assume that our material is homogeneous and isotropic (i.e., polycrystalline) and we consider an object with spherical symmetry, that is formed by a spherical core of radius R, embedded in an infinite matrix that constitutes the external environment. This infinite matrix simulates the coupling of the nanoparticle with the substrate through the streptavidin-biotin bonding. The spherical symmetry of the system ensures that the displacement field spatially depends only on the radial coordinate r, $\mathbf{u}(\mathbf{r},t) = u(r,t)\ \mathbf{u_r}$. The Navier equation becomes

$$\rho\frac{d^2u}{dt^2} = (\lambda+2\mu)\left[\frac{d^2u}{dr^2} + \frac{2}{r}\frac{du}{dr} - \frac{2u}{r^2}\right] \tag{3.20}$$

This equation depends only on the radial coordinate r.

As for the nanodisks, the eigenmodes correspond to harmonic solutions of radial Navier equation:

$$u(r,t) \ = \ u(r)\exp\left(i\tilde{\omega}t\right) \tag{3.21}$$

where the vibrational frequencies $\tilde{\omega}$ are real or complex valued in the case of free and matrix-embedded particles, respectively. In the matrix case, their imaginary part reflects damping of the vibration mode due to the transfer of mechanical energy to the matrix. As for a macroscopic resonator, the properties of vibrational eigenmodes (i.e., their frequency $\tilde{\omega}$ and displacement field $u(r)$) are thus imposed by the boundary conditions, that is continuity of the displacement and of the radial component of the stress tensor σ_{rr} at the nanoparticle-matrix interface. For a radial mode, σ_{rr} is connected to the field $u(r,t)$ by

$$\sigma_{rr} = (\lambda+2\mu)\frac{du}{dr} + 2\lambda\frac{u}{r} \tag{3.22}$$

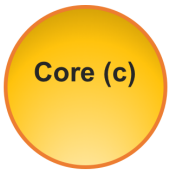

Figure 3.27: Example of a free pure gold nanosphere.

For a free sphere (Figure 3.27), the boundary condition is given by

$$\sigma_{rr}(R) = 0 \tag{3.23}$$

where R is the particle's radius.

Eigenfrequencies are given by

$$\xi \cot \xi = 1 - \frac{\xi^2}{4}\left(\frac{C_L}{C_T}\right)^2 \qquad \text{with} \quad \xi = \frac{\omega R}{C_T} \tag{3.24}$$

In Eq. 3.24, C_L and C_T stand for longitudinal and transversal velocity of sound in the specific material[12], respectively. If we suppose that the nanoparticle is embedded in an infinite matrix, as schematically shown in Fig. 3.28, the Navier equation becomes

$$\xi \cot \xi = 1 - \frac{\xi^2(1 + i\xi/\alpha)}{\eta\xi^2 - 4\alpha^2\gamma^2(1 - 1/\eta\beta^2)(1 + i\xi/\alpha)} \tag{3.25}$$

with

$$\alpha = C_L^{(m)}/C_L^{(c)}, \qquad \beta = C_T^{(m)}/C_T^{(c)}, \qquad \gamma = C_T^{(m)}/C_L^{(m)}, \qquad \eta = \rho^{(m)}/\rho^{(c)}$$

Evaluating the effect of the external environment, there is a weak modification of vibration frequencies, that become lower because of the presence of a matrix around the particle. As we

[12]For the value of constants, see [22]

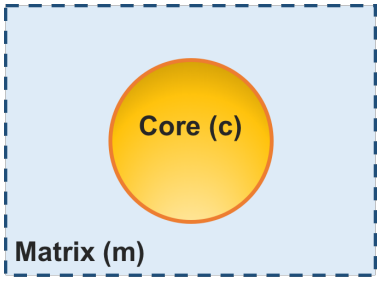

Figure 3.28: Gold nanosphere embedded in a matrix.

will see soon, this is a tiny difference and can be neglected. In this case, the eigenmodes of the nanoparticle are no longer exactly eigenmodes, but *quasi-steady states*, that is particle's modes subject to a damping.

We have found numerically the eigenfrequencies, solving graphically Eqs. 3.24 - 3.25 for ξ_n. The graphic solution is represented in Fig. 3.29. Knowing that $\omega = 2\pi\nu$, eigenfrequencies are calculated as

$$\nu = \frac{\xi \cdot C_L}{2\pi R} \tag{3.26}$$

For a sphere of 20 nm of radius (i.e. the nominal radius of our nanoparticles) the frequencies ν, corresponding to the fundamental breathing mode and to the first eigenmodes, $n = 0$ and $n = 1$ respectively, are

$$\nu_0 = 75.93\ GHz \qquad \text{for} \qquad n = 0$$
$$\nu_1 = 159.7\ Ghz \qquad \text{for} \qquad n = 1$$

for the model with free particle, and

$$\nu_0 = 75,89\ GHz \qquad \text{for} \qquad n = 0$$
$$\nu_1 = 159.7\ GHz \qquad \text{for} \qquad n = 1$$

for the matrix-embedded one's.

As we have done for the nanodisks, now we compare these frequencies with the frequencies of particle's mechanical oscillations obtained analyzing the SVD eigenvectors. For sample E, we have computed a Fast Fourier Transform (FFT) of the residual between eigenvector $\mathbf{u_1}$ and the

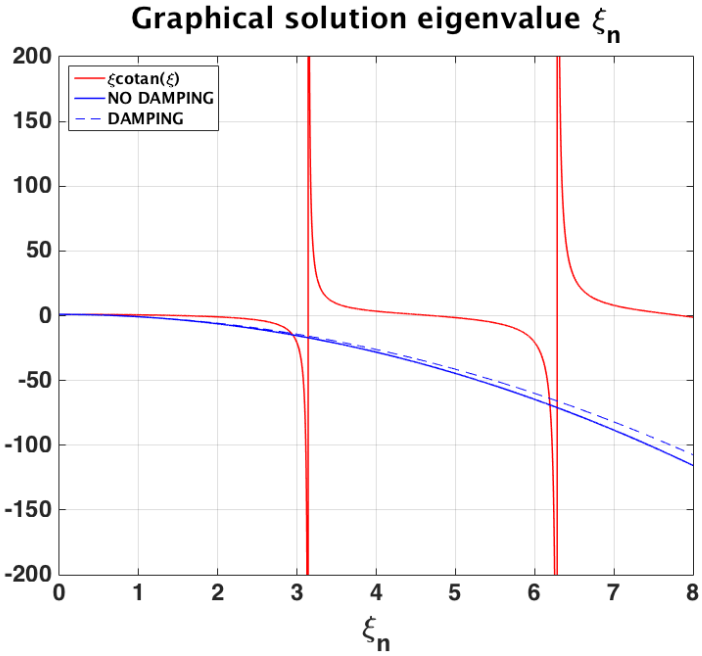

Figure 3.29: Graphical representation of functions $\xi \cot \xi$ (red trace), $1 - \frac{\xi^2}{4}\left(\frac{C_L}{C_T}\right)^2$ (blue continuos line) and real part of $1 - \frac{\xi^2(1+i\xi/\alpha)}{\eta\xi^2 - 4\alpha^2\gamma^2(1-1/\eta\beta^2)(1+i\xi/\alpha)}$ (blue dashed line) . The values of ξ are given by the intersection points. As we can see, there is a minimal difference between the two solutions.

triple-exponential fit performed. For sample A, the FFT is been directly calculated on eigenvector $\mathbf{u_2}$.

In Fig. 3.30 is shown the residual of eigenvector $\mathbf{u_1}$ and its power spectrum. In a similar way, in Fig. 3.31 is reported the eigenvector $\mathbf{u_2}$ and its power spectrum. Only one frequency (around 68 GHz) obtained from the DFT is comparable with those obtained solving the Navier equation. For this reason, we assume that the oscillations in the residual of eigenvector $\mathbf{u_1}$ (i.e., sample E) are due to the excitation of the first eigenmode of a single nanosphere. We can infer similar conclusion for the sample A.

As for the nanodisks, we have performed a fit using a linear combination of two damped sines:

$$f(t) = A \exp\left(-\frac{t}{\tau_1}\right) \sin\left(\frac{2\pi}{T_1}t + \phi_1\right) + B \exp\left(-\frac{t}{\tau_2}\right) \sin\left(\frac{2\pi}{T_2}t + \phi_2\right) \tag{3.27}$$

In Fig. 3.32 is reported the mechanical fit of the residual of eigenvector $\mathbf{u_1}$ for sample E. In Fig.

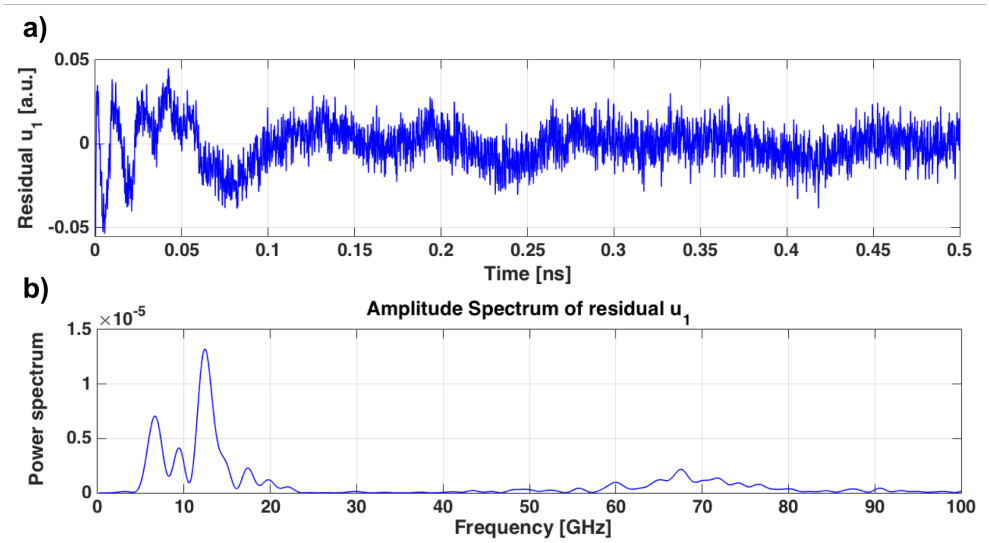

Figure 3.30: (a) shows the residual of eigenvector $\mathbf{u_1}$ versus delay time for the sample E, obtained from the fit represented in Fig. 3.24. In (b) we can see the power spectrum of (a). We can observe three peaks (6.7, 12.5 and 68 GHz). At the two DFT peaks with higher frequencies correspond the two oscillators in (a). Only one frequency (68 GHz) is comparable with those obtained solving the Navier equation (Eq. 3.20).

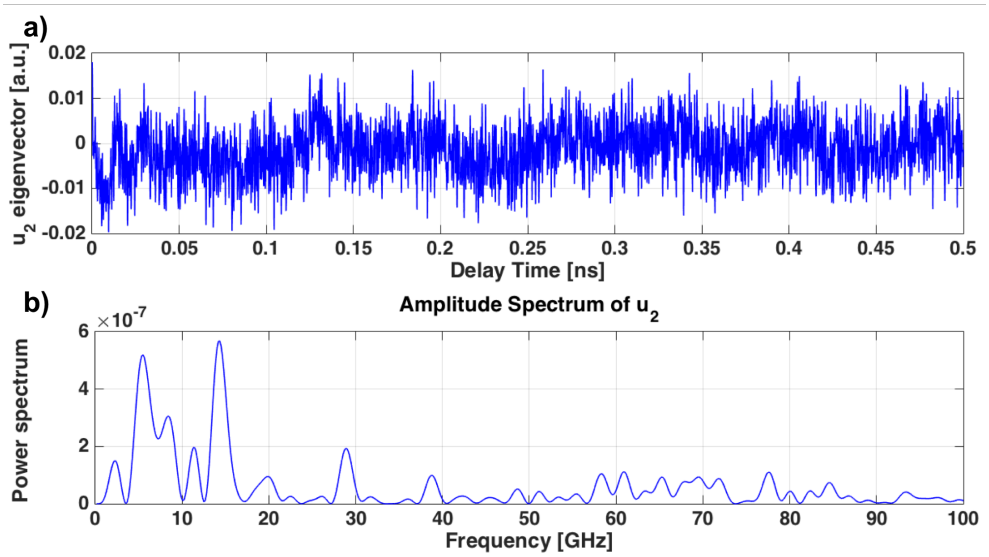

Figure 3.31: (a) shows the eigenvector $\mathbf{u_2}$ versus delay time for the sample A. In (b) we can see the power spectrum of (a). The eigenvector $\mathbf{u_2}$ is more noisy with respect to the residual of eigenvector $\mathbf{u_1}$ and so we have many peaks in DFT. The important thing is that in (b) are also present all the frequencies that appear in Fig. 3.30 (b).

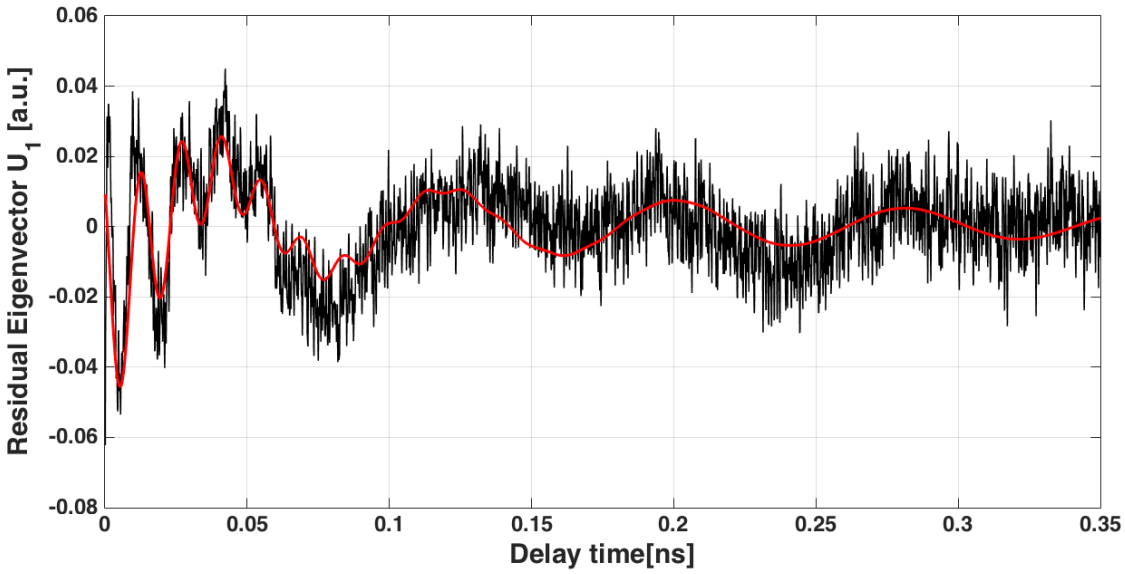

Figure 3.32: In black: the residual of eigenvector $\mathbf{u_1}$ versus delay time up to 350 *ps* for sample E. In red: fit curve obtained with the linear combination of two damped sines.

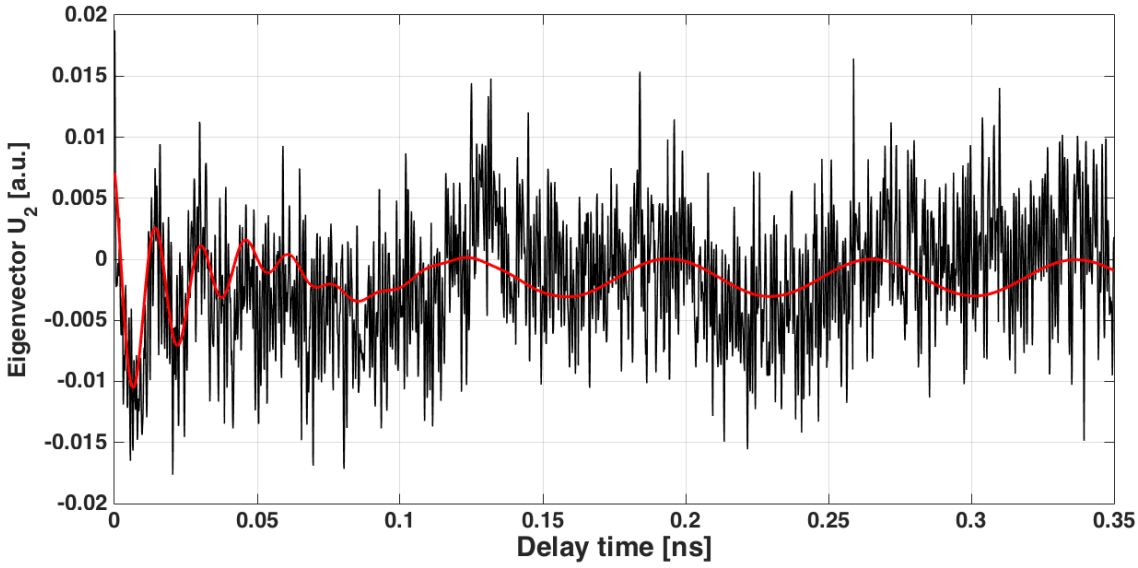

Figure 3.33: In black: eigenvector $\mathbf{u_2}$ versus delay time up to 350 *ps*. In red: fit curve obtained with the linear combination of two damped sines.

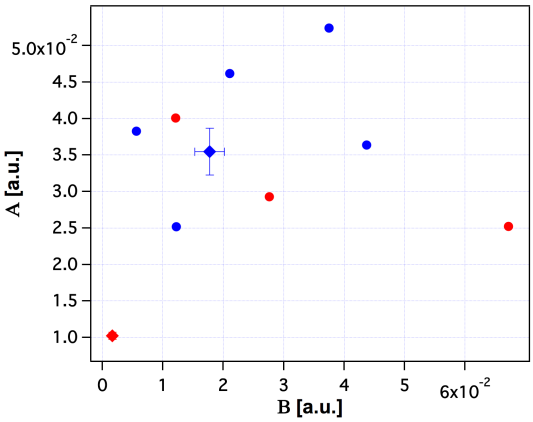

(a) A vs B

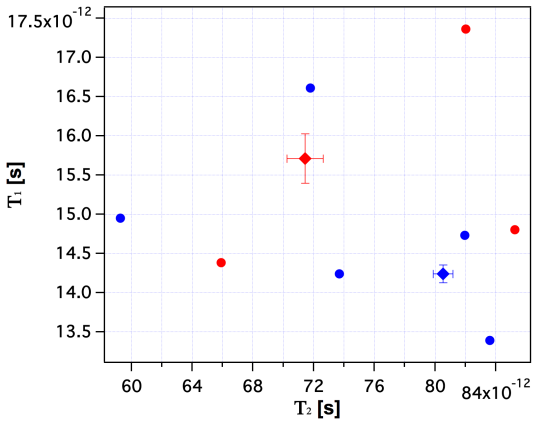

(b) T_1 vs T_2

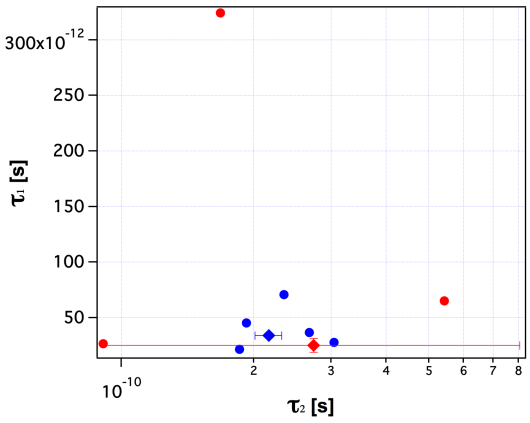

(c) τ_1 vs τ_2

Figure 3.34: Amplitude A, temporal period T and rate of decay τ for the first oscillator versus same coefficients for the second one for each experimental trace. Red markers represent the values corresponding to the sample A, while blue dots the ones corresponding to the sample E. The red square marker represents the value (with the corresponding error bars) obtained from the curve fitting of residual of eigenvector $\mathbf{u_1}$. The blue square marker represents the value (with the corresponding error bars) obtained from the curve fitting of eigenvector $\mathbf{u_2}$.

3.33 is shown the mechanical fit of the eigenvector $\mathbf{u_2}$ for sample A. As for the thermal analysis, we are interested in fit coefficients[13], amplitude A, temporal period T and rate of decay τ, for each oscillators of both dilutions sample. Plotting the fit coefficients of each experimental trace

[13]The complete coefficients tables (with the corresponding confidence interval) are reported in Table C.7 and Table C.8 (see Appendix C).

in a scatter plot and confronting these with the SVD's one, we obtain the graphs in Fig. 3.34.

Looking at the graphs, we can infer that it is not possible to identify a real trend to cluster, therefore such a kind of analysis does not allow us to distinguish one sample from the other. The projection of the experimental traces into a sub-space spanned by the first three eigenvectors allows a more clearly identification of the two dilutions. (Fig. 3.21)

With respect to the thermal part, the fit coefficients of the SVD only partly capture the global trend of the measurements. In particular, the amplitudes A and decays τ. This is easily explained, the amplitude and the dump of the oscillations are partly lost in the singular value decomposition. Furthermore, a fit that is a linear combination of two damped sines is more sensitive than a linear combination of exponentials. In fact, the data analysis program has to find the right combination of phases.

If we analyze the periods T_1 and T_2, the SVD value represent an average of the values for the single measures. These periods are comparable with the frequencies of the DFT and, in particular T_1, with the numerical solution of the Navier equation.

We conclude that the study of the first eigenvectors extracted from the SVD allows us to analyze the thermomechanical dynamic of this nanosystem.

3.2.2 Hierarchical cluster analysis

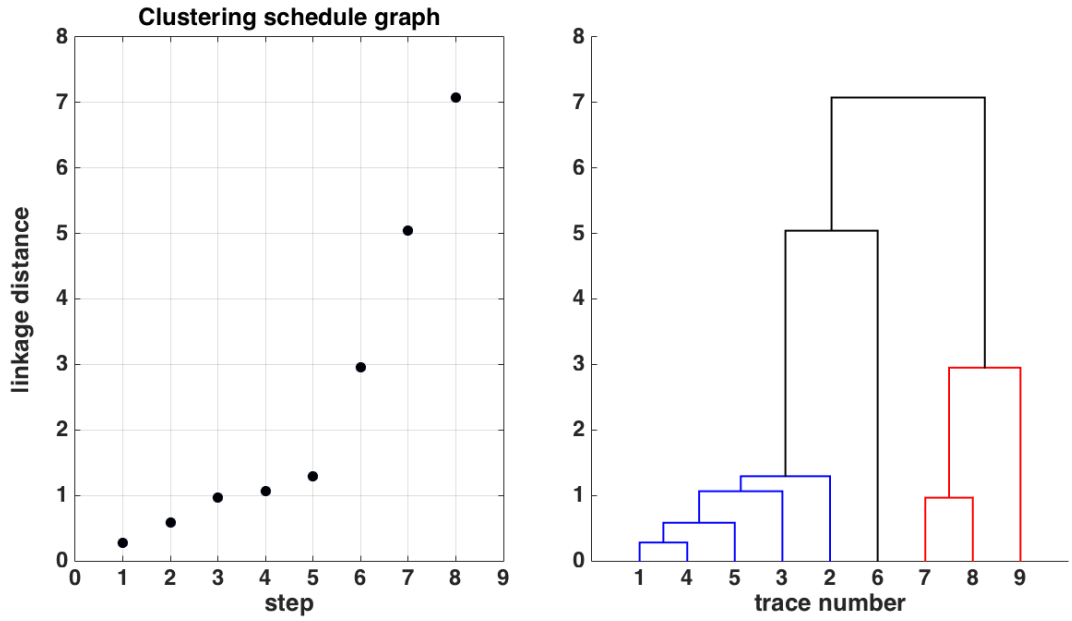

Figure 3.35: Hierarchical cluster analysis. Dendrogram obtained using the Ward's method. The vertical lengths between nodes are proportional to the linkage distance. In blue: cluster related to pure gold nanoparticles measures (i.e., sample E). In red: cluster linked to the sample with 1:10 diluition (i.e, sample A).

The result of hierarchical clustering applied to the nanospheres' measurements is presented in the dendrogram shown in Fig. 3.35[14]. The data group in two distinct clusters, each associated to a single dilution. Thus, this algorithm allows to reveal the internal similarities in the experimental data, in particular, it is able to distinguish the different dilutions of our samples.

Observing Fig. 3.35, we can infer two important conclusions. First of all, the cluster associated to the sample E has a linkage distance smaller with respect to the sample A one's. Therefore, the blue traces are more similar among them than the red one's. This fact has already been observed considering the value of Shannon entropy. For sample E the Shannon entropy was smaller than the sample A. This confirms the efficacy of the mathematical tools used in this works.

The second observation is that the trace 6 do not cluster. For this reason, trace 6 has been excluded from the analysis.

[14]The MATLAB® code used to perform this analysis is presented in Appendix B.2.

In conclusion, with this hierarchical cluster analysis we are able to evidence small differences in the experimental traces. These differences reflect changes in the physical properties of the system. Therefore, analyzing these differences in the data, we can also able to study the physics of the system.

Chapter 4

Conclusions and future perspectives

The aim of this thesis is extract useful information about thermomechanical dynamics of complex systems through a Singular Value Decomposition (SVD) analysis and a hierarchical binary cluster tree dendrogram, starting from single nano-object time-resolved optical measurements. First of all, these statistical tools have been applied to a well-known system like gold/titanium nanodisks made by electronic beam lithography. For such system an analytical model for the thermal dynamics has already been developed. Studying the gold nanodisks we have optimized the mathematical and numerical platform. Next, we have investigated a more complex biological object like gold nanoparticles immobilized on a functionalized surface through the strong chemical bond between biotin and streptavidin.

For both these samples, we have reduce the data dimensions by projecting the original data into a subspace spanned by the eigenvectors with higher relative weight. In this way we have been able to identify tiny differences in the experimental traces, like the diameter's size for the nanodisks or the dilution for the nanoparticles' samples. Similar results have been obtained with the hierarchical cluster analysis. We also studied the thermal and mechanical dynamics of these nano-objects, starting from the analysis of SVD eigenvectors. For the thermal dynamic, we obtain informations about amplitude and rate of decay of exponentials.

Afterwards, the study of mechanical dynamics has been presented, obtaining the oscillation

periods and the corresponding relaxation times. We have estabilished that the frequencies obtained from the SVD analysis and the theoretical values given by solving the Navier equation are comparable. Confronting the fit coefficients related to SVD eigenvectors with those obtained by a standard analysis, we have shown that SVD provides a global analysis, that is able to capture the dynamics of our systems.

Although these analysis allow us to make interesting considerations, there are some aspects that can be improved in the future. First of all, it would be interesting to characterize the nanospheres' samples performing a TEM[1] imaging. Then, it would be interesting to increment the number of measurements analyzed. In this way we would be able to consolidate the technique results for further applications.

In the next future, the SVD analysis could be implemented as a pre-analysis platform, having demonstrated that is able to evidence those measures affected by casual or systematic errors.

[1] Transmission Electron Microscope.

Appendix A

Electronics and devices

A.1 High-speed Photodetector

Let's describe the characteristics of electronic devices used for data acquisition. The Balanced Amplified Photodetector Thorlabs PDB430A is characterized by two channels, reason why we define it as *differential photodetector*. Both the ASOPS system and the technique adopted require this kind of detector in order to acquire the signal difference between the intensity of the transmitted and the reference beam. The technical specifications of these devices satisfy the needed requirements. In particular, we need an high temporal resolution and a low noise.

A.1.1 Differential Photodetector: PDB430A

Thorlabs PDB4xx series Balanced Amplified Photodetectors consist of two well-matched photodiodes and an ultra-low noise, high-speed transimpendance amplifier that generates an output voltage (RF OUTPUT) proportional to the difference between the photocurrents in the two photodiodes, i.e. the two optical input signals. Additionally, the unit has two monitor outputs (MONITOR+ and MONITOR-) to observe the optical input power levels on each photodiode separately.

Figure A.1 shows a functional block diagram of the PDB4xx series balanced amplified photodetectors.

The PDB4xx series is powered by external power supply ($\pm 12\ V$, $200\ mA$). The main features

of photodetector are related in Tables A.1 and A.2. Table A.1 lists common technical data of the PDB4xx series, while Table A.2 lists the individual features of Thorlabs PDB430A. To avoid damaging the photodiodes, it is important to monitor beams' intensity.

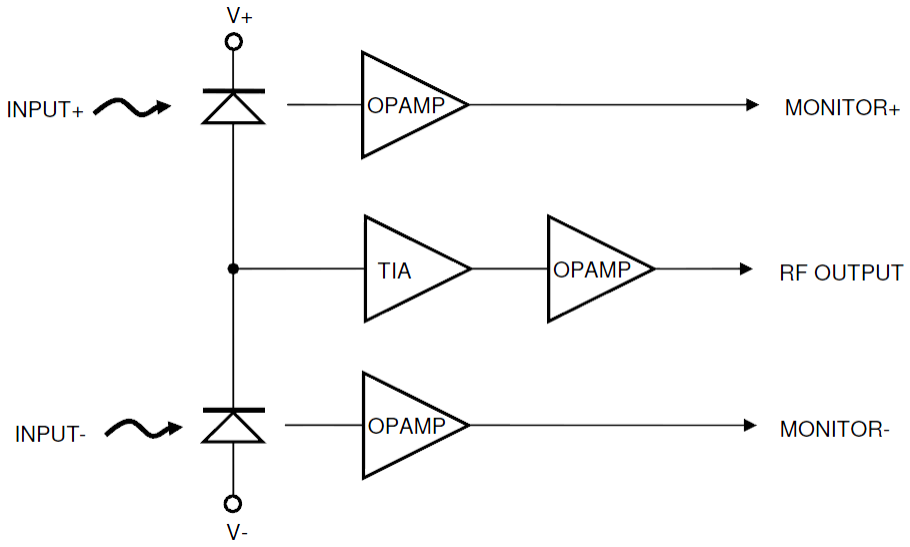

Figure A.1: PDB4xx Series Functional block diagram

Common Technical Data - PDB4xx Series	
Max. Input Power	20 mW (photodiode damage threshold)
RF-Output Impendance	50 Ω
RF OUTPUT voltage swing, max.	± 3.6 V (high impendance load)
Monitor Output Impendance	220 Ω
Monitor Output Bandwidth	DC 1 MHz
Conversion Gain Monitor Outputs	10 V/mW @ peak responsivity
Monitor Output voltage noise	180 μV RMS
DC-offset MONITOR Outputs	¡ ± 2 mV
Size	85x80x30 mm^3
Power Supply	± 12 V, 200 mA

Table A.1: Common features of PDB4xx Series. All technical data are given at 23 ± 5 °C and 35 ± 15% relative humidity.

Individual Technical Data - Thorlabs PDB430A	
Detector Material/Type	Si / PIN
Wavelenght Range	320 nm - 1000 nm
Typical Max. Responsivity	0.5 A/W
Detector Diameter	0.4 mm
RF-Output Bandwidth (3dB)	DC - 350 MHz
Transimpendance Gain	10 x 103 V/A
Conversion Gain RF-Output	$5x10^3$ V/W
CW Saturation Power	720 μW @ 820 nm
Overall output voltage noise	1.5 mV RMS

Table A.2: Individual features of Thorlabs PDB430A

Appendix B

Matlab Codes

B.1 SVD

In this appendix is shown the MATLAB® code for the singular value decomposition analysis performed in this thesis work.

```
clear
clc
close all

addpath(genpath('/your data path/Misure_Ns_bio.txt'))
load('/your data path/Misure_Ns_bio.txt')

M=Misure_Ns_bio; % Data Matrix

t=100.* (1:length(M(:,12)))*1e-6; %time scaling in ns
deltat=100*1e-6; %delta t in ns

Au1D=M(:,7);
Au2D=M(:,8);
Au3D=M(:,9);


X=M(:,(7:9));
```

```
19
20 d=length(X(1,:));
21 floor=mean(X(1:1500,:));
22
23 % normalize
24 X2=[];
25 for nn=1:d
26 X1=X(:,nn)-floor(nn);
27 X2=[X2,X1];
28 end
29 X=X2;
30
31 %%%%%%%%%%%%%%%%%%%%%%%%%%%%%%%%%%%%%%%%%%%%%%
32
33 [mm,ii]=max(X);
34
35 X2=[];
36 X1=[];
37 for nn=1:d
38
39 X1=X(ii(nn):(ii(nn)+35000-1),nn)/mm(nn);
40 X2=[X2,X1];
41 end
42 X=X2;
43
44 % decimation points
45
46 N_dcm=35000;
47 N_points=35000;
48 dcm=round(N_points/N_dcm);
49
50 X_d=[];
51 for nn=1:d
52 X_x=decimate(X(:,nn),dcm,4);
53 X_x=X_x/max(X_x);
54 X_d=[X_d,X_x];
55 end
56
57 t_d=cumsum(ones(N_dcm,1))*(N_points*deltat)/N_dcm; %in ns
```

```
58
59 %%%%%%%%%%%%%%%%%%%%%% SVD %%%%%%%%%%%%%%%%%%%%%%%%%%
60
61 [U,S,V] = svd(X_d,0);
62
63 %population matrix or principal components scores
64
65 M=S*V.';
66
67
68 %%%%%%%%%%%%%%%%%%%%%%%%%%%%%%%%%%%%%%%%%%%%%%%%%%%%%
69
70 % Eigenvectors plots
71
72 figure(1)
73
74 subplot(231)
75 plot(t_d,X_d)
76 grid on
77
78 subplot(232)
79 semilogy(diag(S)/max(diag(S)),'o','MarkerSize',6,'MarkerFaceColor','b')
80 grid on
81 axis([0 20 1e-2 1])
82
83 subplot(233)
84 plot(V(:,1:2).')
85 grid on
86
87 subplot(234)
88 plot(t_d,U(:,1))
89 grid on
90 title('U1')
91
92 subplot(235)
93 plot(t_d,U(:,2))
94 grid on
95 title('U2')
96
```

```
97  subplot(236)
98  plot(t_d,U(:,3))
99  grid on
100 title('U3')
101
102 %%%%%%%%%%%%%%%%%%%%%%%%%%%%%%%%%%%%%%%%%%%%%%%%%%%%
103
104 %Coordinates Plots
105
106 figure(2)
107
108 subplot(131)
109 ll1=1;
110 ll2=2;
111
112 labels = cellstr(num2str([1:3]'));
113 plot(M(ll1,1:3).',M(ll2,1:3).','or','MarkerSize',5,'MarkerFaceColor','r')
114 text(M(ll1,1:3).', M(ll2,1:3).', labels,'FontSize',10,'Color','r',...
115     'FontWeight','bold','VerticalAlignment',...
116     'bottom','HorizontalAlignment','right')
117 grid on
118 hold on
119
120
121 axis equal
122 hold off
123 xlabel('M1')
124 ylabel('M2')
125
126 subplot(132)
127 ll1=1;
128 ll3=3;
129
130 labels = cellstr(num2str([1:3]'));
131 plot(M(ll1,1:3).',M(ll3,1:3).','or','MarkerSize',5,'MarkerFaceColor','r')
132 text(M(ll1,1:3).', M(ll3,1:3).', labels,'FontSize',10,'Color','r',...
133 'FontWeight','bold','VerticalAlignment',...
134 'bottom','HorizontalAlignment','right')
135 grid on
```

```
136 hold on
137
138 axis equal
139 hold off
140 xlabel('M1')
141 ylabel('M3')
142
143 subplot(133)
144 ll2=2;
145 ll3=3;
146
147 labels = cellstr(num2str([1:3]'));
148 plot(M(ll2,1:3).',M(ll3,1:3).','or','MarkerSize',5,'MarkerFaceColor','r')
149 text(M(ll2,1:3).', M(ll3,1:3).', labels,'FontSize',10,'Color','r',...
150 'FontWeight','bold','VerticalAlignment',...
151 'bottom','HorizontalAlignment','right')
152 grid on
153 hold on
154
155 axis equal
156 hold off
157 xlabel('M2')
158 ylabel('M3')
159
160 %%%%%%%%%%%%%%%%%%%%%%%%%%%% Fit 3 exp %%%%%%%%%%%%%%%%%%%%%%%%%%%%%%%%%%%%
161
162 Signal2=-U(:,1)/max(-U(:,1));
163
164 cut_time=3.5; %Cutting time in ns
165 for nn = 1:length(t_d)
166          tdCalc(nn) = abs(t_d(nn) - cut_time);
167 end
168 [idx idx]=min(tdCalc);
169 Signal2=Signal2(1:idx,1);
170 t_d_cut3=t_d(1:idx,1);
171
172 s = fitoptions('Method','NonlinearLeastSquares',...
173                'Startpoint',[0.9 -1000 0.5 -10 0.2 -1]);
174 f = fittype('a*exp(b*x)+c*exp(d*x)+e*exp(f*x)','options',s);
```

```
175
176 [SS_fit_3exp,gof,output] = fit(t_d_cut3,Signal2,f)
177
178 cc3=coeffvalues(SS_fit_3exp);
179
180 S_fit_3exp=cc3(1)*exp(cc3(2)*t_d_cut3)+cc3(3)*exp(cc3(4)*t_d_cut3)...
181     +cc3(5)*exp(cc3(6)*t_d_cut3);
182 tau1=abs(1/cc3(2));
183 tau2=abs(1/cc3(4));
184 tau3=abs(1/cc3(6));
185 tau3exp=[tau1 tau2 tau3]
186
187 Res3=Signal2-S_fit_3exp;
188
189 figure(3)
190 subplot(311)
191 plot(SS_fit_3exp,t_d_cut3,Signal2,'-k','fit')
192 grid on
193 title('Fit-3exp')
194 xlabel('Delay time [ns]')
195 ylabel('Signal [a.u.]')
196
197 subplot(312)
198 plot(t_d_cut3,Res3)
199 grid on
200 title('residui-3exp')
201 xlabel('Delay time [ns]')
202 ylabel('Residual [a.u.]')
203
204 %%%%%%%%%%%%%%%% Fourier transform Res U1  %%%%%%%%%%%%%%%%%%
205
206 N=length(t_d_cut3);
207 deltat=mean(diff(t_d_cut3)); %in ns
208 Fs=1/deltat;
209 NFFT = 2^nextpow2(10*N);
210
211 df=Fs/NFFT; %in GHz
212 f=df*(1:NFFT);
213
```

```
214 NFFT = 2^nextpow2(10*N);
215 Res3_f = fft(detrend(Res3),NFFT);
216
217 mss_Res3_f=abs(Res3_f).^2/N^2;
218
219 %%%%%%%% Plot %%%%%%%%%%%%%%%
220
221 subplot(313)
222 plot(f,mss_Res3_f)
223 v=axis;
224 xlim([0 100]);
225 title('Signal Amplitude Spectrum of Res3')
226 xlabel('Frequency [GHz]')
227 ylabel('Power spectrum')
228 grid on
229
230 %%%%%%%%%%%%%%%%%%%%%%%%%% Fit 2 seni smorzati %%%%%%%%%%%%%%%%%%%%%%%%%%
231 cut_time=0.350; %Cutting time in ns
232 for ii = 1:length(t_d)
233          tdCalc(ii) = abs(t_d(ii) - cut_time);
234 end
235 [idx idx]=min(tdCalc);
236 U2=U(1:idx,2);
237 t_d_cut4=t_d(1:idx,1);
238
239 SU2=smooth(U2,5,'rlowess');
240
241
242 s = fitoptions('Method','NonlinearLeastSquares',...
243                'Startpoint',[0.02 -5 65 +pi/2 0.02 -5 13 -pi/2 0]);
244 f = fittype('a*exp(b*x)*sin(2*pi*c*x+d)+f*exp(g*x)*sin(2*pi*h*x+l)+s',...
245     'options',s);
246
247 [SS_fit_2sin,gof,output] = fit(t_d_cut4,SU2,f)
248
249 cc3=coeffvalues(SS_fit_2sin);
250
251 S_fit_2sin=cc3(1)*exp(cc3(2)*t_d_cut4).*sin(2*pi*cc3(3)*t_d_cut4+cc3(4))...
252     +cc3(5)*exp(cc3(6)*t_d_cut4).*sin(2*pi*cc3(7)*t_d_cut4+cc3(8))+cc3(9);
```

```
253 T1=abs(1/cc3(3));
254 T2=abs(1/cc3(7));
255
256 T2sin=[T1 T2]
257
258 figure(4)
259
260 plot(SS_fit_2sin,t_d_cut4,SU2,'-k','fit')
261 grid on
262 title('Fit-2sin')
263 xlabel('Delay time [ns]')
264 ylabel('Residual [a.u.]')
265 hold on
266
267 %%%%%%%%%%%%%%% Fourier transform U2  %%%%%%%%%%%%%%%%%%
268 signal=U(:,2);
269
270 cut_time=0.5; %Cutting time in ns
271 for nn = 1:length(t_d)
272          tdCalc(nn) = abs(t_d(nn) - cut_time);
273 end
274 [idx idx]=min(tdCalc);
275 signal1=signal(1:idx,1);
276 t_d_cut=t_d(1:idx,1);
277
278
279 N=length(t_d_cut);
280 deltat=mean(diff(t_d_cut)); %in ns
281 Fs=1/deltat;
282 NFFT = 2^nextpow2(10*N);
283
284 df=Fs/NFFT; %in GHz
285 f=df*(1:NFFT);
286
287 NFFT = 2^nextpow2(10*N);
288 U1_f = fft(detrend(signal1),NFFT);
289
290 mss_U1_f=abs(U1_f).^2/N^2;
291
```

```
292 %%%%%%%% Plot %%%%%%%%%%%%%%%
293
294 figure(5)
295 subplot(212)
296 plot(f,mss_U1_f)
297 v=axis;
298 title('Signal Amplitude Spectrum of U2')
299 xlabel('Frequency [GHz]')
300 ylabel('Power spectrum')
301 xlim([0 100])
302 grid on
303
304 subplot(211)
305 plot(t_d_cut,signal1,'k')
306 xlabel('Delay Time [ns]')
307 ylabel('Signal [a.u.]')
308 grid on
309
310
311 %%%%%%%%%%%%%%%%%%%%%%%%%%%%  Autocorrelation %%%%%%%%%%%%%%%%%%%%%%%%%%%%
312
313 figure(6)
314
315 for ii=1:3
316 [xc,lags] = xcorr(U(:,ii),5000,'coeff');
317
318 conf99 = sqrt(2)*erfcinv(2*.05/2);
319 lconf = -conf99/sqrt(length(t_d));
320 upconf = conf99/sqrt(length(t_d));
321
322
323 subplot(3,1,ii)
324
325 stem(lags,xc,'filled')
326 ylim([lconf-0.4 1.05])
327 hold on
328 plot(lags,lconf*ones(size(lags)),'r','linewidth',2)
329 plot(lags,upconf*ones(size(lags)),'r','linewidth',2)
330 title(['Eigenvector U_' num2str(ii) ' Autocorrelation (95% C.I.)'])
```

```
331 xlabel('Lag')
332 ylabel('Autocorrelation')
333 end
```

B.2 Hierarchical cluster analysis

In this appendix is shown the MATLAB® code for the Hierarchical cluster analysis performed in this thesis work.

```
close all

addpath(genpath('/your data path/Misure_Ns_bio.txt'))
load('/your data path/Misure_Ns_bio.txt')

M=Misure_Ns_bio; % Data Matrix

t=100.* (1:length(M(:,12)))*1e-6; %time scaling in ns
deltat=100*1e-6; %delta t in ns

Au1D=M(:,7);
Au2D=M(:,8);
Au3D=M(:,9);


X=M(:,(7:9));

%%%%%%%%%%%%%%%% Dendrogram  %%%%%%%%%%%%%%%%%%

distance=pdist(X.');
dendo=linkage(distance,'ward');


figure (5)
subplot(121)
plot(dendo(:,3,:),'ob','MarkerSize',9,'MarkerFaceColor','b')
title('Clustering schedule graph')
xlabel('step')
ylabel('linkage distance')
v=axis;
%axis([v(1) v(2) 0 19])


```

```
34 subplot(122)
35 dendrogram(dendo,'colorthreshold','default')
36 v=axis;
37 %axis([v(1) v(2) 0 15])
38 xlabel('sample number')
39 hold on
```

Appendix C

Tables of curve fit coefficients

Gold Nanodisks: Thermal analysis

trace number	τ_1 [fs]	τ_2 [ps]	τ_3 [ns]	A [a.u.]	B [a.u.]	C [a.u.]
1	1400 (1041, 2160)	166 (126, 244)	2.17 (1.95, 2.44)	1.23 (0.79, 1.67)	0.14 (0.12, 0.16)	0.28 (0.26, 0.29)
2	519 (324, 1290)	125 (77, 321)	1.44 (1.34, 1.56)	4.38 (0.79, 9.54)	0.08 (0.05, 0.10)	0.29 (0.27, 0.30)
3	780 (554, 1320)	133 (83, 347)	1.42 (1.31, 1.55)	2.36 (0.99, 3.73)	0.07 (0.05, 0.10)	0.27 (0.25, 0.29)
4	1730 (1447, 1478)	195 (165, 239)	2.51 (2.31, 2.75)	1.11 (0.90, 1.31)	0.16 (0.14, 0.17)	0.27 (0.26, 0.29)
5	966 (680, 1670)	178 (115, 394)	1.48 (1.34, 1.67)	1.76 (0.85, 2.68)	0.10 (0.07, 0.12)	0.29 (0.26, 0.31)
SVD	1090 (929, 1310)	166 (141, 204)	1.78 (1.70, 1.87)	1.56 (1.25, 1.86)	0.11 (0.10, 0.12)	0.28 (0.27, 0.29)

Table C.1: Values of amplitude and rate of decay, one for each exponential, obtained from the fit of the measurements performed on the 100 nm nanodisk. In round brackets, the corresponding 95% confidence interval.

trace number	τ_1 [fs]	τ_2 [ps]	τ_3 [ns]	A [a.u.]	B [a.u.]	C [a.u.]
6	420 (230, 2430)	294 (203, 530)	1.32 (1.18, 1.50)	5.07 (-5.06, 15.20)	0.13 (0.08, 0.19)	0.40 (0.34, 0.45)
7	122 (-8.4e-8, 8.4e-8)	161 (103, 368)	1.14 (1.06, 1.23)	174 (-2e6, 2e6)	0.14 (0.10, 0.18)	0.54 (0.50, 0.58)
8	826 (542, 1730)	300 (217, 483)	1.35 (1.20, 1.55)	1.48 (0.42, 2.54)	0.18 (0.12, 0.23)	0.42 (0.35, 0.48)
9	752 (431, 2960)	169 (119, 294)	1.22 (1.15, 1.30)	1.52 (-0.14, 3.18)	0.13 (0.10, 0.16)	0.50 (0.47, 0.53)
SVD	556 (356, 1270)	212 (166, 292)	1.22 (1.17, 1.29)	2.41 (-0.11, 4.93)	0.13 (0.11, 0.16)	0.48 (0.45, 0.50)

Table C.2: Values of amplitude and rate of decay, one for each exponential, obtained from the fit of the measurements performed on the 90 nm nanodisk. In round brackets, the corresponding 95% confidence interval.

Gold Nanodisks: Mechanical analysis

trace number	τ_1 [ps]	τ_2 [ps]	T_1 [ps]	T_2 [ps]	A [a.u.]	B [a.u.]
1	460 (264, 580)	245 (121, 366)	58.2 (57.3, 59.1)	125 (116, 135)	0.05 (0.03, 0.07)	0.03 (0.01, 0.05)
2	1311 (503, 2155)	3773 (329, 3.9e5)	54.3 (53.8, 54.9)	102 (98, 107)	0.04 (0.03, 0.05)	0.017 (0.004, 0.030)
3	572 (339, 733)	1430 (360, 3.9e3)	54.8 (54.2, 55.4)	100 (97, 103)	0.05 (0.04, 0.07)	0.02 (0.01, 0.04)
4	955 (536, 1107)	549 (288, 782)	65.8 (65.3, 66.4)	118 (114, 123)	0.04 (0.03, 0.05)	-0.02 (-0.04, -0.02)
5	2452 (650, 7442)	313 (154, 463)	54.6 (54.1, 55.2)	102 (97, 108)	-0.04 (-0.06, -0.03)	-0.03 (-0.06, -0.01)
SVD	389 (285, 609)	88 (60, 162)	54.6 (54.2, 55.1)	117 (107, 129)	0.04 (0.03, 0.05)	-0.05 (-0.06, -0.03)

Table C.3: Values of amplitude, rate of decay and period, one for each damped sine, obtained from the fit of the measurements performed on the 100 nm nanodisk. In round brackets, the corresponding 95% confidence interval.

trace number	τ_1 [ps]	τ_2 [ns]	T_1 [ps]	T_2 [ps]	A [a.u.]	B [a.u.]
6	335 (244, 535)	2.46 (-0.41, 11.31)	53.3 (52.8, 53.8)	96 (93, 99)	-0.07 (-0.09, -0.06)	-0.02 (-0.03, -0.01)
7	453 (243, 627)	1.99 (-0.21, 13.51)	53.0 (52.1, 53.0)	101 (96, 107)	-0.07 (-0.09, -0.04)	-0.024 (-0.047, -0.001)
8	364 (243, 570)	0.92 (-0.34, 1.22)	52.9 (52.4, 53.3)	93 (91, 96)	-0.08 (-0.10, -0.07)	-0.02 (-0.04, -0.02)
9	364 (269, 733)	8.26 (-0.38, 169.43)	52.2 (51.8, 52.8)	91 (88, 95)	-0.08 (-0.10, -0.06)	-0.02 (-0.04, -0.01)
SVD	393 (890, 971)	1.88 (-0.50, 1.08)	52.8 (52.4, 53.1)	95 (93, 97)	0.078 (0.067 0.089)	-0.022 (-0.031 -0.013)

Table C.4: Values of amplitude, rate of decay and period, one for each damped sine, obtained from the fit of the measurements performed on the 90 nm nanodisk. In round brackets, the corresponding 95% confidence interval.

Gold Nanosferes: Thermal analysis

trace number	τ_1 [fs]	τ_2 [ps]	τ_3 [ns]	A [a.u.]	B [a.u.]	C [a.u.]
1	907 (863, 954)	82 (81, 84)	2.09 (1.88, 2.34)	0.92 (0.89, 0.95)	0.300 (0.297, 0.304)	-0.013 (-0.014, -0.012)
2	1240 (1188, 1290)	79 (77, 81)	1.56 (1.34, 1.86)	0.93 (0.90, 0.95)	0.232 (0.228, 0.235)	-0.008 (-0.009, -0.007)
3	976 (931, 1024)	72 (70, 73)	0.91 (0.80, 1.07)	0.76 (0.74, 0.79)	0.326 (0.323, 0.329)	-0.010 (-0.012, -0.009)
4	1510 (1494, 1530)	75 (74, 75)	1.75 (1.69, 1.85)	0.81 (0.80, 0.82)	0.308 (0.307, 0.309)	-0.0082 (-0.0085, -0.0079)
5	1620 (1556, 1680)	81 (78, 82)	0.99 (0.85, 1.16)	0.92 (0.90, 0.95)	0.258 (0.255, 0.262)	-0.012 (-0.014, -0.011)
SVD	1250 (1220, 1270)	77 (76, 78)	1.50 (1.41, 1.59)	0.85 (0.83, 0.86)	0.287 (0.286, 0.289)	-0.010 (-0.011, -0.009)

Table C.5: Values of amplitude and rate of decay, one for each exponential, obtained from the fit of the measurements performed on the sample E. In round brackets, the corresponding 95% confidence interval.

trace number	τ_1 [fs]	τ_2 [ps]	τ_3 [ns]	A [a.u.]	B [a.u.]	C [a.u.]
7	844 (781, 917)	75 (72, 78)	4.79 (-0.36, 6.02)	0.99 (0.94, 1.06)	0.23 (0.22, 0.24)	-0.0044 (-0,0056, -0.0037)
8	1030 (965, 1110)	73 (71, 76)	0.60 (0.18, 4.74)	0.91 (0.87, 0.96)	0.28 (0.28, 0.29)	-0.0016 (-0,0058, -0,0025)
9	947 (878, 1030)	67 (64, 71)	1.43 (0.90, 3.51)	0.96 (0.90, 1.01)	0.19 (0.18, 0.20)	-0.0040 (-0.0058, -0.0025)
SVD	929 (890, 971)	73 (71, 74)	1.68 (1.23, 2.65)	0.957 (0.957, 0.987)	0.236 (0.232, 0.239)	-0.0035 (-0.045, -0.0026)

Table C.6: Values of amplitude and rate of decay, one for each exponential, obtained from the fit of the measurements performed on the sample A. In round brackets, the corresponding 95% confidence interval.

Gold Nanosferes: Mechanical analysis

trace number	τ_1 [ps]	τ_2 [ps]	T_1 [ps]	T_2 [ps]	A [a.u.]	B [a.u.]
1	67 (57, 80)	229 (206, 257)	14.7 (14.6, 14.8)	81.5 (81.0, 82.0)	-0.038 (-0.042, -0.033)	-0.044 (-0.047, -0.042)
2	46 (40, 54)	180 (152, 221)	14.2 (14.1, 14.3)	73.7 (72.8, 74.6)	0.045 (0.040, 0.050)	0.021 (0.018, 0.023)
3	36 (29, 49)	292 (217, 445)	16.5 (16.2, 16.8)	72.1 (71.2, 73.1)	0.025 (0.021, 0.030)	0.012 (0.009, 0.014)
4	28 (25, 32)	254 (226, 291)	15.0 (14.9, 15.2)	59.7 (59.4, 59.9)	0.038 (0.034, 0.041)	-0.0049 (-0.0055, -0.0043)
5	21 (18, 28)	185 (163, 215)	13.2 (12.9, 13.5)	83.1 (82.3, 83.9)	0.051 (0.043, 0.059)	0.037 (0.034, 0.041)
SVD	34 (30, 39)	216 (190, 251)	14.2 (14.1, 14.3)	80.5 (79.8, 81.1)	-0.035 (-0.039, -0.032)	0.018 (0.016, 0.019)

Table C.7: Values of amplitude, rate of decay and period, one for each sine, obtained from the fit of the measurements performed on the sample E. In round brackets, the corresponding 95% confidence interval.

trace number	τ_1 [ps]	τ_2 [ps]	T_1 [ps]	T_2 [ps]	A [a.u.]	B [a.u.]
7	351 (251, 585)	159 (141, 182)	17.3 (17.3, 17.4)	83.6 (82.8, 84.4)	-0.024 (-0.028, -0.020)	-0.069 (-0.074, -0.063)
8	59 (49, 75)	444 (322, 715)	14.5 (14.3, 14.6)	66.1 (65.5, 66.7)	-0.043 (-0.049, -0.037)	-0.011 (-0.013, -0.009)
9	22 (15, 43)	93 (69, 145)	14.4 (13.7, 15.1)	83.4 (79.9, 87.3)	0.036 (0.023, 0.049)	-0.026 (-0.033, -0.019)
SVD	25 (890, 971)	273 (-559, 947)	15.7 (15.4, 16.0)	71.4 (70.2, 72.6)	-0.010 (-0.012, -0.008)	0.0016 (0.0012, 0.0021)

Table C.8: Values of amplitude, rate of decay and period, one for each sine, obtained from the fit of the measurements performed on the sample A. In round brackets, the corresponding 95% confidence interval.

Appendix D

Acronyms and symbols

ASOPS *ASynchronous Optical Sampling*

CCD *Charge-Coupled Device*

HR *High Reflectivity*

PBS *Phosphate Buffered Saline*

SPM *Scanning Probe Microscopy*

DFT *Discrete Fourier Transform*

FFT *Fast Fourier Transform*

EBM *Electron Beam Lithography*

FWHM *Full Width at Half Maximum*

δU *Energy density absorbed from pump pulse*

$\Delta\nu$ *Detuning frequency*

T_{osc} *Oscillation period*

T *Temperature*

ΔT *Temperature variation*

P *Power*

A *Amplitude*

I *intensity*

R *Radius of the particle*

D *Diameter of the particle*

σ_{ext}	*Effective cross section*
ν	*Frequency*
f	*Focal lenght*
λ	*Wave length*
τ	*Rate of decay*
ρ	*Mass density*
ω	*Angular frequency*
ϕ	*Phase*
κ	*Thermal conductivity*
w_0	*Minimum waist*
z_0	*Quote of minimum waist*
$a.u.$	*Arbitrary Unit*

Bibliography

[1] L.R. Hirsch, R.J. Stafford, J.A. Bankson, S.R. Sershen, B. Rivera, R.E. Price, J.D. Hazle, N.J. Halas, and J.L. West, *Proc. Natl. Acad. Sci. U. S. A* **100**, 13549 (2003).

[2] P.K. Jain, I.H. El-Sayed, and M.A. El-Sayed, *Nanotoday* **2**, 18 (2007).

[3] L. Paasonena, T. Laaksonenb, C. Johansb, M. Yliperttulac, K. Kontturib, and A. Urttic, *J. of Controlled Release* **122**, 86 (2007).

[4] Science **338**, 936 (2012).

[5] Phys. Chem. **Chem. Phys.**, 2013. Accepted Manuscript. DOI: 10.1039/C2CP43771F.

[6] Nano Lett. **11**, 4126 (2011).

[7] F. Medeghini, "Time resolved microscopy on nanostructured materials", Tesi di Laurea in Fisica, Università Cattolica del Sacro Cuore, A.A. 2011-2012.

[8] A. Sterzi, "Time resolved microscopy on nanostructured materials", Tesi di Laurea Magistrale in Fisica, Università Cattolica del Sacro Cuore, A.A. 2011-2012.

[9] C. Giannetti, B. Revaz, F. Banfi, M. Montagnese, G. Ferrini, F. Cilento, S. Maccalli, P. Vavassori, G. Oliviero, E. Bontempi, L. E. Depero, V. Metlushko, and F. Parmigiani,*Phys. Rev. B* **76**, 125413 (2007).

[10] www.quartz-silica.net/sapphire.htm.

[11] L. Sola, M. Chiari (2012) *J. Chromatogr. A*, **1270**: 324-329

[12] A. Ronchi, "Termomeccanica impulsiva di un singolo nanodisco", Tesi di Laurea Triennale in Fisica, Università Cattolica del Sacro Cuore, A.A. 2012-2013.

[13] O. Alter, P. O. Brown, D. Botstein, *Singular value decomposition for genome-wide expression data processing and modeling*, *PNAS* **2000**, textit97 (18), 10101-10106,

[14] C. E. Shannon, *A Mathematical Theory of Communication*, Bell System Technical Journal, **27** (3) 379?423 (1948)

[15] G. Bianchetti, "Time-resolved optical investigation of gold nanospheres immobilized on a functionalized surfaces for biological applications", Tesi di Laurea Triennale in Fisica, Università Cattolica del Sacro Cuore, A.A. 2014-2015.

[16] F. Banfi, F. Pressacco, B. Revaz, C. Giannetti, D. Nardi, G. Ferrini and F. Parmigiani, *Phys. Rev. B* **81** 155426 (2010).

[17] A. Canteri, "Studio di fattibilità di una microscopia ottica risolta in tempo basata su tecnica ASOPS", Tesi di Laurea Triennale in Fisica, Università Cattolica del Sacro Cuore, A.A. 2010-2011.

[18] M.J. Weber *Handbook of optical materials* CRC Press, 2003.

[19] F. Pressaco *Studio di fattibilità per una tecnica completamente ottica per misure nanocalorimetriche*, Università degli Studi di Trieste, Master Thesis (2008); http://www.dmf.unicatt.it/elphos/.

[20] M. E. Wall, A. Rechtsteiner, L. M. Rocha, *Singular value decomposition and principal component analysis*, extracted from the book: D. Berrar, W. Dubitzky, M. Granzow, *A Practical Approach to Microarray Data Analysis*, Springer US, pp. 91 - 109.

[21] V. Juvé, A. Crut, P. Maioli, M. Pellarin, M. Broyer, N. Del Fatti and F. Vallée *Probing elasticity at the nanoscale: THz acoustic vibrations of nanometric platinum particles*, LASIM, CNRS-Université Lyon 1

[22] A. Crut, V. Juvé, D. Mongin, P. Maioli, N. Del Fatti and F. Vallée (May 26, 2011) *Physical Review B* **83**, 205430 (2011)

[23] V. Juvé, A. Crut, P. Maioli, M. Pellarin, M. Broyer, N. Del Fatti and F. Vallée (2010) *Nano Lett.* **2010**, textit10, 1853-1858, DOI:10.102/nl100604r

[24] http://www.thorlabs.de/thorproduct.cfm?partnumber=PDB430A-AC.

[25] Stoner1993: R. J. Stoner and H. J. Maris, Phys. Rev B 48, 16373 (1993).

[26] Siemens, M. E.; Li, Q.; Yang, R.; Nelson, K. A.; Anderson, E. H.; Murnane, M. M.; Kapteyn, H. C. Nat. Mater. 2010, 9, 26.

[27] Menlo System, *ASOPS white paper*, April 15 2009.

[28] M. Travagliati, *Fabrication and time-resolved optical investigation of hypersonic phononic crystals*, Università Cattolica del Sacro Cuore, Master Thesis (2007); http://www.dmf.unicatt.it/elphos/.

[29] V. Hartland, *Chem. Rev.* **111**, 3858 (2011).

[30] Thorlabs Instrumentation Operation Manual; http://www.atom.fysik.lth.se/QI/laser_documentation/Manuals/Photodetectors/PDA10BS-AC,%20Thorlabs/TL_PDA10Bx.pdf.

[31] Thorlabs Instrumentation Operation Manual; http://www.phy.davidson.edu/fachome/dmb/-RESolGelGlass/manuals/ThorlabDetectors.pdf.

[32] Catalog Datasheet Piezo Nano Positioning; http://www.physikinstrumente.com/en/pdf/-P611_XZ_Datasheet.pdf.

[33] http://www.edmundoptics.com/imaging/imaging-lenses/fixed-magnification-lenses/nikon-cfi-60-infinity-corrected-brightfield-objectives/2690.

[34] E. D. Palik, *Handbook of Optical Constants of Solids*, Academic Press, 1191.

[35] C. Torrence and G. P. Compo, *A Pratical Guide to Wavelet Analysis*, Bulletin of the American Meteorological Society, Vol. 79, No. 1, January 1998.

[36] G. Chen, Nanoscale energy transport and conversion, Oxford University Press, 2005.

Ringraziamenti

Ringrazio il mio relatore Prof. Gabriele Ferrini, il Prof. Francesco Banfi e tutti coloro che mi hanno assistito in questo lavoro di tesi, specialmente il Dr. Simone Peli, Giada Bianchetti e Andrea Sterzi, che si sono sempre resi disponibili nell'aiutarmi.

Un ringraziamento va a tutti i miei famigliari, in particolare a mamma, papà e Matteo che mi hanno supportato in questi anni; un grazie sincero, perché forse senza di loro non avrei ottenuto gli stessi risultati. Il loro sostegno è stato fondamentale nei momenti più difficili e i loro molti sacrifici mi hanno dato la grande possibilità di formarmi culturalmente come persona. Una parte di questo successo è merito loro, e di questo glie ne sarò sempre grato.

Grazie a tutti gli amici climbers, e in particolare a Pedro, Fabio, Compagno pappagallo, Boris, Dido, Luke e Sasha, con i quali ho condiviso e spero di condividere ancora molte avventure per crode e pareti. Superare difficoltà e potenziali pericoli insieme, mi ha aiutato ad apprezzare le piccole gioie di tutti i giorni con un sorriso in più.

Grazie a tutte quelle persone, troppe per essere ringraziate singolarmente, con cui ho condiviso questi meravigliosi anni universitari e che hanno reso speciale e indimenticabile ogni singolo giorno.